

Structural materials

Design considerations for high entropy alloys in advanced nuclear applications



Michael Moschetti^a, Patrick A. Burr^a, Edward Obbard^a, Jamie J. Kruzic^a, Peter Hosemann^b, Bernd Gludovatz^{a,*}

^a School of Mechanical and Manufacturing Engineering, UNSW Sydney, Sydney, NSW 2052, Australia

^b Department of Nuclear Materials, University of California, Berkeley, CA 94720, USA

ARTICLE INFO

Article history:

Received 19 August 2021

Revised 28 April 2022

Accepted 24 May 2022

Available online 26 May 2022

Keywords:

High entropy alloys

Nuclear materials and applications

Fission and fusion

Ashby maps

Periodic table

ABSTRACT

The demanding operating environments of advanced nuclear reactors require the development of new nuclear materials that can withstand their increased physical, chemical, thermal, and radiation-related challenges. High-entropy alloys (HEAs) have shown often-impressive mechanical, thermomechanical, and corrosion-resistant properties, and offer a massive, unexplored compositional space which allows for the targeted development of application-specific materials. Furthermore, although still in a nascent stage, research has shown that HEAs may exhibit unique irradiation tolerance, including reduced defect production and resistance to irradiation-induced swelling and hardening. The mechanisms behind this increased tolerance are not yet well-understood, although the HEA-specific attributes of a complex energy landscape, reduced thermal conductivity, and shift in defect migration energies and pathways provide promising explanations. This work assesses the current and future challenges faced by structural nuclear materials, identifying the specific applications in which HEAs may provide a competitive advantage compared to industry-standard materials with the aid of Ashby material selection maps. Considerations are provided for the design of future nuclear HEAs, including calculations of nuclear-relevant properties to assist in the initial down-selection of elements depending on application requirements (e.g., low neutron capture for in-core applications), narrowing the existing compositional space of HEAs to a manageable scope.

© 2022 Elsevier B.V. All rights reserved.

1. Introduction

Advanced structural materials are key to the continued development of reliable, sustainable, and efficient advanced nuclear reactors – both fission and fusion. Generation IV (Gen-IV) fission and proposed fusion reactor designs will operate under unprecedented conditions. In both cases, components are expected to experience temperatures up to and exceeding 1000 °C, new corrosive environments (e.g., liquid metals, molten salts, gases, super-critical fluids), and/or larger and harder neutron fluences than seen in current generation reactors. Fusion has the additional challenge of exposing the materials to extreme magnetic fields while exposing the first wall to a plasma and helium ion bombardment leading to temperature excursions and surface erosion phenomena. Economy and safety dictate that some of these components must operate for a lifetime of 60 years without failure. Particle accelerators could

also benefit greatly from improved materials that can better handle exposure to radiation, temperature, and stress simultaneously to enable higher power on targets. Material properties considerations include radiation damage resistance, corrosion resistance, and sufficient mechanical properties (e.g., strength, creep, creep-fatigue, ductility retention) over the operating temperature range. Additionally, minimization of radiological activation reduces the complexity and cost of decommissioning by reducing the amount of hazardous materials that require disposal and increases the potential for recycling.

Material damage occurs in nuclear reactors and particle accelerators due to a combination of physical, thermal, radiative, and chemical factors. Although in many cases there are existing materials which can withstand each individual effect, it is a technological challenge to contend with multiple effects simultaneously, especially when such detrimental conditions combine synergistically to greatly enhance the rate of degradation. These factors impose performance limitations, such as reduced component lifetime or a lower operating temperature and efficiency. Neutron irradiation, in particular, proves challenging as the chargeless particles penetrate

* Corresponding author at: UNSW Sydney, Sydney, NSW 2052, Australia.

E-mail address: bgludovatz@unsw.edu.au (B. Gludovatz).

throughout material volumes and cause activation, transmutation, and displacement damage.

Current light-water reactors (LWR) often employ Zr alloys for fuel cladding due to their reduced neutron capture properties, Ni-Cr alloys for high-temperature and heat-transfer applications due to their excellent thermomechanical properties and corrosion resistance, and various low-alloy and stainless steels for components with less demanding property requirements. However, current fission reactors typically operate at no more than 320 °C with a significantly lower lifetime displacement damage when compared to developing technologies [1]. Traditional reactor materials often prove insufficient when considering the demands of future reactor designs. In the search for advanced materials with enhanced performance across the various reactor environments, ferritic-martensitic (F-M) [2] and oxide-dispersion strengthened (ODS) [3] steels, SiC/SiC composites [4], and advanced refractory alloys [5] are among the materials that show promise for various applications. These materials each introduce their own advantages and disadvantages, and many Gen-IV reactors and proposed fusion reactor designs are still hindered by the challenge to develop materials to meet their requirements.

High-entropy alloys (HEAs) have proven to offer some unique and excellent material properties in the ~18 years since their inception. Various compositions have shown impressive mechanical properties [6,7], thermomechanical performance [11–16], and enhanced corrosion resistance [8,17–19]. HEAs exhibit a unique distortion of their atomic lattice which affects heat dissipation, defect production, and defect mobility processes [20–22] to promote defect recombination and annihilation – the so called ‘self-healing’ effect. HEAs composed of refractory elements may be of particular interest to the nuclear community due to their retention of mechanical properties at high temperatures [23,24] which is a key challenge in many advanced nuclear applications.

Here, we review HEAs for use in nuclear applications and discuss what HEA-specific phenomena may be exploited to develop materials with, for example, improved radiation-tolerance, low activation, or enhanced high-temperature performance. Additionally, we highlight where HEAs could fill technological gaps that exist due to the shortcomings of existing materials such as corrosion resistant fuel claddings which improve accident tolerance, or reduced activation in-core components which decrease the burden on reprocessing, decommissioning and disposal. Finally, we provide element-specific data on critical nuclear properties which aids in the down-selection of compositional components and thereby the development of new HEAs for use across the various challenging applications in future nuclear reactors.

1.1. The current and near-future nuclear materials landscape

Current generation fission reactors are almost all thermal reactors, typically operating at temperatures around 300 °C and experiencing up to ~70 displacements per atom (dpa) in locations with relatively high amounts of radiation exposure over their lifetime [25]. These reactors (Generation II–III+) use low-alloy steels (e.g., SA508, SA533) and austenitic stainless steels (e.g., 304, 309, 316/316LN) in applications with low to medium neutron flux such as pressure vessels and piping, providing strength, toughness, corrosion-resistance, and good manufacturability at a relatively low cost. For higher temperatures, Ni- and Fe-based superalloys (e.g., A286, X750) are used for their creep resistance. Zr alloys (e.g., Zircaloy-4, Zircaloy-2, Zr1%Nb, Zr2.5%Nb) are used for fuel cladding and core structural components due to their low neutron capture cross sections combined with suitable mechanical strength and corrosion resistance.

Materials in Gen-IV reactor designs will experience more severe conditions, for instance core-outlet temperatures seen in the

sodium-cooled fast reactor (SFR) are expected to reach 550 °C while the very high temperature reactor (VHTR) is expected to operate at or above 1000 °C. Corrosion-resistance in Gen-IV reactor technologies is further complicated due to the array of differing corrosion and passivation mechanisms seen for the different coolants (i.e., liquid metals, molten salts, gases, and super-critical water). The lifetime irradiation-induced damage seen in some components of these reactors is expected to exceed 200 dpa [1].

Components in fusion reactors may face operating temperatures up to 1000 °C and 200 dpa in one service lifetime [25]. While neutron irradiation-induced damage and extreme operating temperatures are issues shared between fission and fusion applications, these are also somewhat dissimilar due to the 14.1 MeV neutrons produced in a deuterium-tritium fusion reaction and the cryogenic environments required for the superconducting magnets. Critical challenges in the plasma-facing components concern plasma instabilities which can deliver rapid, intense pulses of energy (up to ~10 MW m⁻²) that ablate exposed components [26]. Bombardment by neutrons, ions and particles from the plasma sputters material back into the plasma, contaminating and potentially quenching it. High-Z elements are known to sputter less but have a higher capacity for quenching, conversely, low Z elements sputter more but are less likely to quench the plasma. Due to their thermomechanical properties, high Z materials for these plasma-facing components include refractory alloys containing W and V while low Z materials include Be and C/C composites [27].

In many cases ideal materials for components in advanced nuclear reactors have not yet been identified or the already identified materials require improvements to achieve design targets.

2. Radiation damage and mitigation mechanisms in HEAs

HEAs are defined primarily by their multiple principal element constitution, typically consisting of 5 or more elements in equiatomic or near-equiatomic ratio [28]. Random distribution of these constituent element atoms with their varying atomic radii gives rise to distortion of the crystal lattice as illustrated in Fig. 1. This results in the introduction of significant interatomic forces and an irregular distribution of energy potentials, creating a complex energy landscape (Fig. 1). The distorted lattice structure of HEAs may assist in the recombination of defects and improve the mechanical properties of the material [29–31].

2.1. Displacement damage and defect migration

While initial recovery following a collision cascade occurs rapidly (within tens of picoseconds), some residual defects remain as a function of temperature, and these are commonly used as a measure of radiation damage [33–35]. HEAs may provide increased irradiation-tolerance by enhancing the initial damage recovery process. Zhang *et al.* [22,29] found that increasing chemical complexity in the Ni-based system (Ni to NiCrFeCo(Mn or Pd)) resulted in a reduced capability to dissipate incident energy due to the differing 3d electron counts of the constituent elements and a subsequent reduction of the electron mean free path, which resulted in greater localized heating and subsequent greater defect recombination capacity. Local variations in atomic radii of the randomly distributed constituents gives rise to distortion of the lattice (Fig. 1; left) which results in significant atomic level stresses and the formation of a more complex energy landscape (Fig. 1; right) [21,22,32,36]. Significant atomic level stresses may result in a greater defect recombination capacity due to increased localized melting and amorphization caused by local heat spikes [22]. Parkin *et al.* [37] attributed reduced defect production in a NbTaTiV alloy compared to pure V to changes in heat transport during the thermal spike due

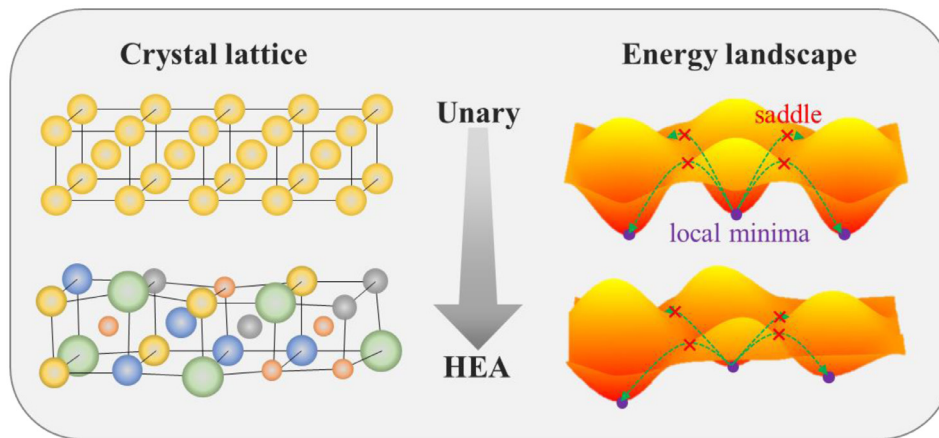


Fig. 1. Crystal lattice distortion and the complex energy landscape developed by increasing compositional complexity from unary alloys to high-entropy alloys (HEAs). The energy landscape highlights the diverse interatomic potentials that result from the compositional complexity; adapted from [32].

to greatly increased scattering of phonons and electrons in HEAs compared to less compositionally complex materials and a subsequent decrease of the mean-free path during the transport of heat from the displacement cascade.

Migration of radiation-induced point defects into larger defect structures such as voids or dislocation loops causes macroscopic property and physical changes (i.e., swelling, creep, embrittlement, etc.) [38]. Vacancy-interstitial recombination reduces the buildup of all types of non-equilibrium defects. Alloys that exhibit a more complex energy landscape, such as HEAs and other disordered alloys with large atomic size differences, may exhibit enhanced defect recombination due to a shift in atomic migration from one-dimensional to three-dimensional motion. Lu *et al.* [21] observed this shift both by molecular dynamic (MD) simulations and experimentally in pure-Ni and Ni-containing alloys with 2-5 constituent elements, finding that increased alloy complexity reduced defect mobility and altered migration pathways, confining defects to localized zones and increasing the chances of defect recombination.

The existence and significance of sluggish diffusion in HEAs are debated [39], in part due to the experimental difficulty of directly measuring diffusion. While several experimental and computational approaches have measured a reduced diffusion coefficient with increasing number of constituents [40–43], such sluggish diffusion likely depends to a greater degree on the specific alloy constituents than on the compositional complexity of HEAs [44–48]. One contribution to sluggish diffusion is thought to arise from the complexity of the HEA lattice energy landscape that more effectively traps and blocks atomic migration, and therefore as a consequence of lattice distortion and local chemical environment. These mechanisms of sluggish diffusion would have the potential to slow point defect agglomeration and retard creep, enhancing the in-reactor performance of HEAs. In this regard, the molecular dynamics of Jin *et al.* [32] suggest that a minimum in the mixing energy and a complex energy landscape can slow down the clustering of interstitial defects, leading to higher defect recombination. Furthermore, a greater mobility reduction of interstitials and interstitial loops compared to vacancies in a vacancy-supersaturated solution may enhance defect recombination in HEAs, reducing swelling [22].

On the other hand, Chen *et al.* [49] found that, at low irradiation temperatures (<300 °C), CrMnFeCoNi, $\text{Al}_{0.3}\text{CrFeCoNi}$ and 316H steel all experience similar radiation-induced hardening when exposed to the same irradiation treatment, concluding that sluggish diffusion and high configurational entropy had minimal influence on the HEAs. However, the $\text{Al}_{0.3}\text{CrFeCoNi}$ HEA ordered into

an L_{12} phase during irradiation, which is known to significantly increase hardness. Such results highlight that although the complex energy landscape of HEAs might provide improvements to defect production and migration, this is but one factor in alloy design. A similar argument can be made from the results of Kumar *et al.* [50] who reported that medium-entropy alloy (MEA) CrMnFeNi, irradiated between room temperature and 700°C, had similar irradiation-induced hardening to 316 steel. While the MEA exhibited a much higher density of smaller dislocation loops than 316 steel, there was essentially no void formation and limited solute depletion/enrichment at grain boundaries when compared to 316 steel. This suggests a more sluggish solute diffusion in the MEA.

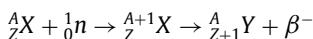
HEAs have demonstrated resistance to swelling during ion beam irradiation. The CrFeCoNiPd (FCC) HEA showed only 0.31% volumetric swelling at 38 ± 5 dpa and 580 °C (~ 0.56 of the melting temperature, T_m) [51] and CrMnFeCoNi (FCC) as little as 0.1% swelling at 60 dpa and 500 °C ($\sim 0.45 T_m$) [21], which represent a two order of magnitude reduction compared to pure nickel irradiated under comparable conditions ($\sim 0.34 T_m$). 316 stainless steels irradiated under such conditions may expect 5–10% swelling while ferritic-martensitic steels, known for their swelling resistance, expect around 1–2%. Yang *et al.* [52] studied pure Ni and Ni-containing alloys composed of 2–5 elements, determining that both greater compositional complexity and specific elemental constitution play significant roles in reducing void swelling, reducing from $\sim 6.7\%$ swelling in pure Ni, to $<0.2\%$ swelling in NiCoFe and NiCoFeCrMn. Typically, reduced swelling is seen in BCC alloys compared to FCC alloys, although some HEA studies found that FCC-structured variations of $\text{Al}_x\text{CrFeCoNi}$ had reduced swelling compared to BCC counterparts [53,54]. Yang *et al.* [53] identified that compositions with a BCC phase had ordered or multiple phases which reduce configurational entropy and structural stability, potentially explaining the variation. Among BCC HEAs, TiZrNbHfTa displayed swelling of 1.23% at >30 dpa and 100 °C [55], typical for refractory elements which often exhibit $<2\%$ swelling [56].

The impact of point defect production and migration on the mechanical properties of a material are dependent on the incident neutron flux, fluence and energy spectrum, and the material temperature [57]. Irradiation-induced hardening and embrittlement is typically seen at low temperatures and saturates at as high as 10 dpa in 316LN [58]. Void swelling, phase instabilities and irradiation creep become a limiting factor at intermediate temperatures ($\sim 0.2\text{--}0.55 T_m$) as migration barriers are reduced and both

atoms and defects migrate more easily [27]. Components such as the fuel assembly, reactor pressure vessel (RPV) and piping of next-generation fission reactors, and the first wall of fusion reactors can be expected to perform at temperatures where void swelling and irradiation creep are dominant phenomena. Enhanced creep resistance has been reported for $\text{Al}_x\text{CrFeCoNi}$ [59] and CrMnFeCoNi [60] HEAs compared to CoNi and Ni, respectively, and was attributed to sluggish diffusion and atomic size differences. Ma *et al.* [61] examined the role of crystal structure using HEA films and found that the BCC alloy $\text{Al}_{2.5}\text{CrFeCoNiCu}$ had significantly greater creep resistance and a six-fold greater activation volume than the FCC CrFeCoNiCu , indicating that BCC-structured alloys may be preferred where creep-resistance is desired. Further reduction to HEA creep rates can be achieved with microstructural approaches such as oxide dispersion strengthening (ODS) or precipitation strengthening. Hadraba *et al.* [62] produced an ODS CoCrFeNiMn HEA that achieved up to a 3 order of magnitude reduction in creep strain rates when tested at 800 °C compared with its non-ODS counterpart. Moreover, Tsao *et al.* [16] reported on a so-called 'high-entropy superalloy' consisting of an FCC matrix and L_{12} ordered precipitates exhibiting thermomechanical properties and creep resistance comparable to some of the most creep-resistant superalloys.

2.2. Transmutation

Incident subatomic particles (e.g., neutrons) may be captured by lattice atoms, altering the isotope. The most common neutron reaction in a thermal flux is capture (n, γ) followed by beta decay (β^-), as follows:



Many others are possible. Both the initial neutron capture, and subsequent decay leave the nucleus in excited states, which revert to ground state by the emission of gamma radiation. Neutron capture cross sections tend to be larger at lower neutron energies, resulting in a more transmutation per incident neutron in a thermal flux. All decaying nuclides can exhibit high activity (short half-life) or extremely long half-lives (low activity); radiation safety considerations seek to reduce the impact of the decay radiation thereby created. The changes to a material's elemental composition alter its functional and mechanical properties, limiting the use of some elements in nuclear applications. While HEAs are susceptible to transmutation, they provide some mitigation to the effects of He – commonly produced by (n, α) reactions – and H – from (n, p) reactions. Due to its insolubility, He collects in vacancy clusters and voids, forming bubbles which reduce ductility while increasing hardness and swelling [63]. HEAs may retard the development and migration of He-bubbles via increased energy barriers reducing the mobility of He interstitials, and increased defect recombination capacity which reduces the number of available vacancies required for vacancy-mediated He migration. Chen *et al.* [64] irradiated pure Ni and FeCoNiCr at 500–700 °C (~ 0.45 – $0.57 T_m$) with 2 MeV He^+ ions. The HEA exhibited a higher density of small He bubbles and a lower bubble volume fraction, attributed to enhanced defect recombination in HEAs and consequently, reduced vacancy concentration which suppresses vacancy-assisted bubble growth. However, further studies including binary and ternary solutions are needed to confirm that this outcome is caused by compositional complexity and not simply a function of the specific elemental constitution. Zhang *et al.* [22] demonstrated that careful tailoring of the HEA composition can narrow the gap between vacancy and interstitial migration energies, further increasing the likelihood of defect recombination. This work suggests HEAs may mitigate the effects of He-bubble formation.

3. Material selection for nuclear components

The pressure vessel of a pressurized water reactor (PWR) requires sufficient mechanical strength to contain the pressure and must be weldable. Fuel cladding requires high neutron-transparency, acceptable mechanical strength, and suitable corrosion resistance. Piping must resist corrosion at high temperatures with acceptably low material costs. Each component should have an optimum material. Yet, components face several demanding factors at once, therefore requiring trade-offs in material selection. For example, adding coating to Zr-based fuel cladding to improve its corrosion resistance reduces reactivity margins.

Of all elements on the periodic table, Miracle and Senkov [39] reported in a 2017 review that four elements (Co, Cr, Fe or Ni) were each in over 70% of the studied HEAs, and only 7% of HEAs were of refractory constitution, which they defined as containing at least 4 of the 9 refractory metal elements: Cr, Hf, Mo, Nb, Ta, Ti, V, W and Zr, plus Al. While recent years have seen an explosion of HEA research, the development of HEAs is still in its infancy. Not all elements can be reasonably used in HEAs without forming simpler binary or ternary crystalline phases (e.g., most non-metallic elements). An initial down-selection of elements of interest can be made by analyzing both element-specific and alloy-specific properties for specific applications. This is especially true for properties that are element-specific, such as neutron transparency or activation, and can therefore be determined for alloys by a rule of mixtures (i.e., as the weighted average of the constituents). Accordingly, such properties will be the focus of the subsequent sections. Mechanical properties, such as strength or toughness, are more challenging to predict due to their alloy-specific nature which depends on complex interactions among the elemental constituents, defects, microstructural features, and deformation mechanisms at various length scales. Our knowledge of the micromechanical mechanisms of deformation and fracture coupled with metallurgical principles can help guide the development of HEAs for nuclear applications. In this context, alloy specific properties will be discussed alongside the element specific properties.

The material selection maps first introduced by M. Ashby [65] compare multiple material properties and a relevant optimization metric of these properties to select materials for individual components. Previously, the general challenges of nuclear environments with materials selections was discussed [66,67] considering conventional available materials. In the following sections we apply this concept and develop several such plots with particular focus given to revealing relationships between failure conditions and the nuclear properties of interest.

3.1. Minimizing neutron capture

Zr alloys such as Zircaloy-4 or Zr-1%Nb have long been the preferred choice for fuel cladding due to their extremely low neutron capture cross section. Significant research has been put into finding replacement materials or a corrosion resistant cladding that can help avoid catastrophic failure of the cladding in the event of an extended station blackout or severe loss-of-coolant accident. Ceramic composites such as SiC/SiC have low neutron capture cross section, high-temperature strength, and irradiation tolerance; however, challenges with fabrication, permeability, corrosion, and toughness have impeded the successful application of SiC/SiC composites in industry. HEAs possess the corrosion resistance, strength, and thermal properties required of an accident-tolerant fuel cladding. Stronger fuel cladding materials can be produced with a reduced thickness, partially offsetting some of their higher cross-section.

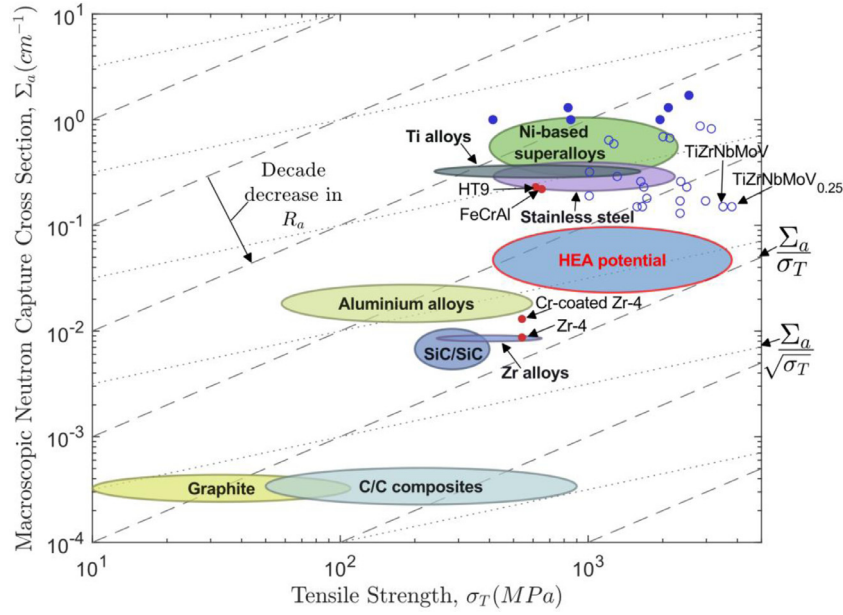


Fig. 2. Tensile strength vs. macroscopic neutron capture cross section for various materials at room temperature. Existing high-entropy alloys are plotted as blue dots (hollow dots are used where only compressive data is available) while potential HEAs are represented as a range, optimized for minimum neutron capture. Dashed and dotted lines represent constant neutron absorption rates for fuel pins (Σ_a/σ_T) and channel boxes ($\Sigma_a/\sqrt{\sigma_T}$), respectively, constrained by burst pressure. Each new line proceeding lower and to the right indicates a decade decrease in neutron absorption rate.

Fig. 2 plots key material groups and several HEAs by their macroscopic cross section for neutron absorption, Σ_a^* , and tensile strength, σ_T . Due to limited reporting on HEA tensile properties, several alloys in Fig. 2 are plotted by their compressive strength (marked by hollow dots). Appendix A3, provides data for the plotted alloys. The 'HEA potential' circle defines an area bounded horizontally by the range of strength suggested by existing HEAs, and vertically by a range of macroscopic neutron capture cross section for elemental mixtures of low cross-section elements considered appropriate for in-core applications (namely, Be, Zr, Cr, V, Ti, Nb, Mo, Fe and Al). The definition preserves HEA mixing rules of 5+ elements mixed with atomic ratio of 5-35 at.% each.

The dashed and dotted lines represent materials of equivalent performance for cladding and channel boxes, defined as the neutron absorption rate, R_a , when constrained by burst pressure. The lines establish a connection between the property that is to be maximized/minimized (neutron absorption rate) and the constraining parameter (burst pressure) through a shared variable (thickness). Eqs. (1-4) apply to hollow tubes (i.e., fuel cladding):

$$R_a = V\Phi\Sigma_a = 2\pi r t l \Phi \Sigma_a \quad (1)$$

where R_a is the neutron absorption rate of the material, and Φ , the neutron flux. The volume, V , of the fuel cladding assumes the walls are suitably thin compared to the overall dimensions (generally, $r > 10t$); r , t , and l represent tube radius, thickness, and length, respectively. The burst pressure of the thin-walled tube is given by:

$$P = \frac{\sigma_T t}{r} \quad (2)$$

where σ_T is the tensile strength of the material. Rearranging Eqn. (2) with respect to t , and substituting this into Eqn. (1), the following relationship is developed, describing neutron absorption

rate as a function of burst pressure:

$$R_a = \{2\pi r^2 l \Phi P\} \left\{ \frac{\Sigma_a}{\sigma_T} \right\} \therefore R_a \propto \frac{\Sigma_a}{\sigma_T} \quad (3)$$

Separating engineering constraints (left) and material properties (right), in Eqn. (3) shows the neutron absorption rate is directly proportional to the macroscopic cross section and inversely proportional to the tensile strength. Lines of constant R_a (i.e., constant $\frac{\Sigma_a}{\sigma_T}$) are included in Fig. 2 as dashed lines, allowing comparison of material choices for a pressure-resisting tube that minimizes neutron absorption [65]. Here, the lines are spaced in logarithmic decades, although any line with the same slope can be drawn to compare materials. The $R_a \propto \Sigma_a/\sigma_T$ relationship furthermore extends to pressure tubes and to RPVs where burst pressure remains the constraining parameter.

This methodology can be expanded to numerous key components in nuclear reactors, such as channel boxes, components which surround the fuel rod assemblies in boiling water reactors (BWRs) to provide structural support and direct water over the fuel rods for cooling. The failure mechanisms for channel boxes include bulging due to the internal/external pressure differential and bowing due to differential irradiation-induced growth of the box sides. For bulging, a relationship similar to fuel pins can be developed between pressure differential and neutron absorption, resulting in the following relationship (derived in Appendix A2) which provides the dotted lines of constant R_a in Fig. 2:

$$R_a \propto \frac{\Sigma_a}{\sqrt{\sigma_T}} \quad (4)$$

From Fig. 2, an initial comparison can be made for applications where minimum neutron absorption is critical such as in-core components in nuclear reactors. Carbon/carbon (C/C) composites exhibit the lowest neutron absorption for both calculated failure conditions. However, their low cross section makes them the most susceptible to increases caused by impurities, and C/C composites have shown significant issues with dimensional stability, porosity, and radiation-induced hardening [68,69].

¹ Determined for each isotope by $\Sigma_a = \sigma N$ and combined at natural abundance to determine elemental values, where N is the atomic number density of the element and σ the thermal-neutron (0.0253 eV) microscopic absorption cross section of each isotope (from [67]).

Fig. 2 reveals that SiC/SiC composites are equal in performance to Zr alloys for cladding and could outperform Zr alloys for channel boxes. From a practical perspective, it is easier to deploy SiC/SiC channel boxes than cladding, as the manufacturing challenges of SiC/SiC are less critical here. HEAs are spread wide along both axes, owing to the number of element combinations for HEAs. Some HEAs are competitive with existing Zr alloys for cladding and pressure tube applications where higher absorption cross-section is compensated by the higher strength, enabling thinner tube construction. Existing HEAs with low neutron absorption rates, TiZrNbMo and TiZrNbMoV_{0.25} (labelled in Fig. 2; [70]), exhibit a single phase BCC structure, exceptional strength, and moderate compressive ductility (30–34% compressive strain at failure) making them competitive among HEAs for cladding. Notably, while some HEAs included in Fig. 2 come close to the ‘HEA potential’ region, no current alloy that has been tested falls within this region. This is due to both limited investigations into low neutron capture HEAs and, where initial investigations have occurred, a lack of mechanical testing and strength data. Furthermore, most existing HEA data are characterized with homogenized microstructures that are not reflective of their equilibrium microstructures at reactor operational temperatures where they might decompose into multiple phases, emphasizing the need for aging experiments at temperatures relevant to reactor operation. HEAs that seek to minimize neutron absorption should make maximum use of Be, Mg, Si, Zr and Al, moderate their use of Zn, Nb, Mo, Fe, Cr, Cu, Ni, V and Ti, and avoid Mn, W, Ta, Co and Hf. Investigations into the AlBeFeSiTi system, such as the lightweight Al₂₀Be₂₀Fe₁₀Si₁₅Ti₃₅ HEA [71] which exhibits 3 intermetallic phases, a high hardness of 8.9 GPa and a low density of 3.91 g cm⁻³, may show promise in this regard, however, the mechanical properties of this alloy have not been thoroughly characterized.

Current fuel utilization – both in terms of burn-up and residence time – is limited chiefly by cladding corrosion from hydrogen pickup. Current Zr-based cladding alloys could be substituted for other materials from the same line of constant R_a for improved fuel utilization, accident tolerance, and/or to allow for increased operating temperatures – all without impacting neutron capture. Current candidate materials for the replacement of Zr-based claddings, such as FeCrAl (labelled in Fig. 2), exhibit notably higher neutron capture, however, this is compensated for by increased strength, heightened accident tolerance, and improved corrosion performance. These plots do not consider all the application-relevant properties and a more in-depth comparison would be needed to account for other properties such as corrosion resistance, creep resistance, thermal stability, and chemical compatibility. Considering the impetus for safety improvements, the excellent corrosion-resistant and radiation-tolerant properties of HEAs, more research on compositions for nuclear applications is justified.

A second Ashby map for the minimization of neutron absorption is shown in Fig. 3 for constraining parameters dependent on Young’s modulus, E , relevant for bowing of channels boxes. Here, the dashed lines of constant R_a are drawn from the following relationship (derived in Appendix A2) allowing for the selection of materials with the lowest possible R_a for square channel boxes constrained by bowing failure:

$$R_a \propto \frac{\Sigma_a}{E} \quad (5)$$

As the Young’s moduli of different materials have less variability than their tensile strength, the relatively higher variability of neutron-capture cross sections is more influential than in Fig. 2. SiC/SiC and C/C composites show a clear advantage. Potential HEAs exhibit very similar neutron capture properties (Σ_a/E) to those of

the Al alloys, both of which are only slightly inferior to Zr alloys in this regard, while other desirable attributes such as radiation-tolerance, corrosion resistance, and thermomechanical properties highlight HEAs as prime candidates for BWR channel boxes.

3.2. Minimizing short- and long-term radioactivity

Radioactive elements release significant energy during and immediately after reactor operation, such as Co which releases several orders of magnitude more gamma energy than most transition metals one day after reactor shutdown. Such elements hinder reactor maintenance by increasing the ‘cool down’ period before maintenance can be safely performed. Other elements retain high activity for long periods of time, such as Nb which remains radioactive after 100,000 years, requiring long term storage. Such elements increase the burden on reprocessing, decommissioning and disposal. Good material selection improves the economy, sustainability, and overall public acceptance of nuclear technology.

3.2.1. Element selection for low activation

The following method aids in the selection of low-activation elements. Fig. 4 gives an overview of the radioactivity profile of elements post-irradiation in the form of a periodic table, determined via nuclear activation and decay calculations [72]. Three irradiation conditions are used. Two fission conditions are characteristic of in-core irradiation in a thermal and fast reactor at fluxes of 10^{14} and 10^{15} n cm⁻² s⁻¹, respectively. The fusion condition is characteristic of irradiation at the first wall of a D-T fusion reactor, at a flux of 10^{15} n cm⁻² s⁻¹. Each irradiation condition is applied for a period of 5 years. Neutron activation calculations are described in Appendix A1. The radioactivity over decay time is given in Fig. 4 for each naturally occurring element, where the details for each element can be understood by referring to the larger inset figure which uses the same axes and limits. The measure of hazard here is contact gamma dose rate (\dot{D}_γ , in Sv h⁻¹), determined from [73]:

$$\dot{D}_\gamma = C \frac{B}{2} \sum_{i=1}^{N_\gamma} \frac{\mu_a(E_i)}{\mu_m(E_i)} S_\gamma(E_i) \quad (6)$$

where C is a conversion factor (from MeV kg⁻¹ s⁻¹ to Sv h⁻¹, $C = 3600 \times 1.602 \times 10^{-13}$) and B is the buildup factor (here given as $B = 2$). The gamma emission spectrum is split into N_γ energy groups with E_i mean energies. For each group, μ_a and μ_m are the coefficients for mass energy absorption of air and mass energy attenuation of the material, respectively, (m² kg⁻¹; obtained from [74]), and S_γ is the gamma emission of the active material (MeV kg⁻¹ s⁻¹). Within each mini-plot, two sets of limits for the safe recycling of active material have been defined according to [75]:

- Remote limit (blue lines) – 10 mSv h⁻¹ after 10 years, indicating the possibility for materials to be processed in dedicated nuclear facilities with appropriate protection measures.
- “Hands-on” limit (red lines) – 10 μSv h⁻¹ after 100 years, indicating the possibility for materials to be processed with minimal radiological protection.

The hands-on limit has significant relevance, as a dose rate of 10 μSv h⁻¹ over a 2000 hour work year results in a 20 mSv dose, which is the annual limit of radiation workers [76]. Alternative limits for recycling, maintenance, and disposal are given by Ref. [77].

Fig. 4 reveals that several elements do not decay to the hands-on limit even after a period of 10,000 years (the upper boundary provided here) regardless of the irradiation condition, with notable exception of low-Z elements which exhibit a combination of very

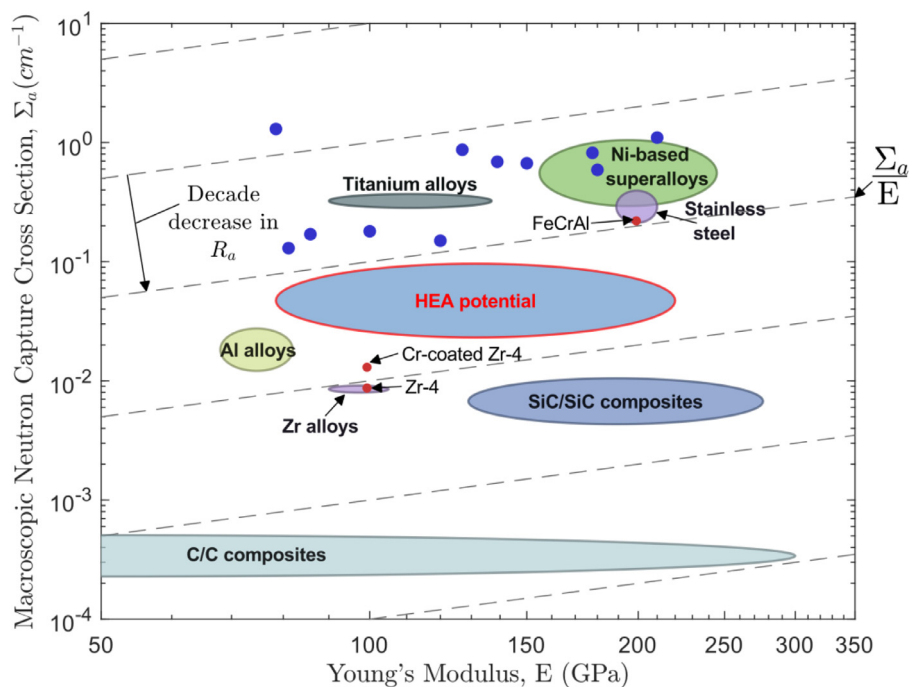


Fig. 3. Young's modulus vs. macroscopic neutron capture cross section for various materials at room temperature. Existing high-entropy alloys are plotted as blue dots while potential HEAs are represented as a range, optimized for minimum neutron capture. Dashed lines represent constant neutron absorption rates (Σ_a/E) for both channel boxes constrained by buckling failure. Each new line proceeding lower and to the right indicates a decade decrease in neutron absorption.

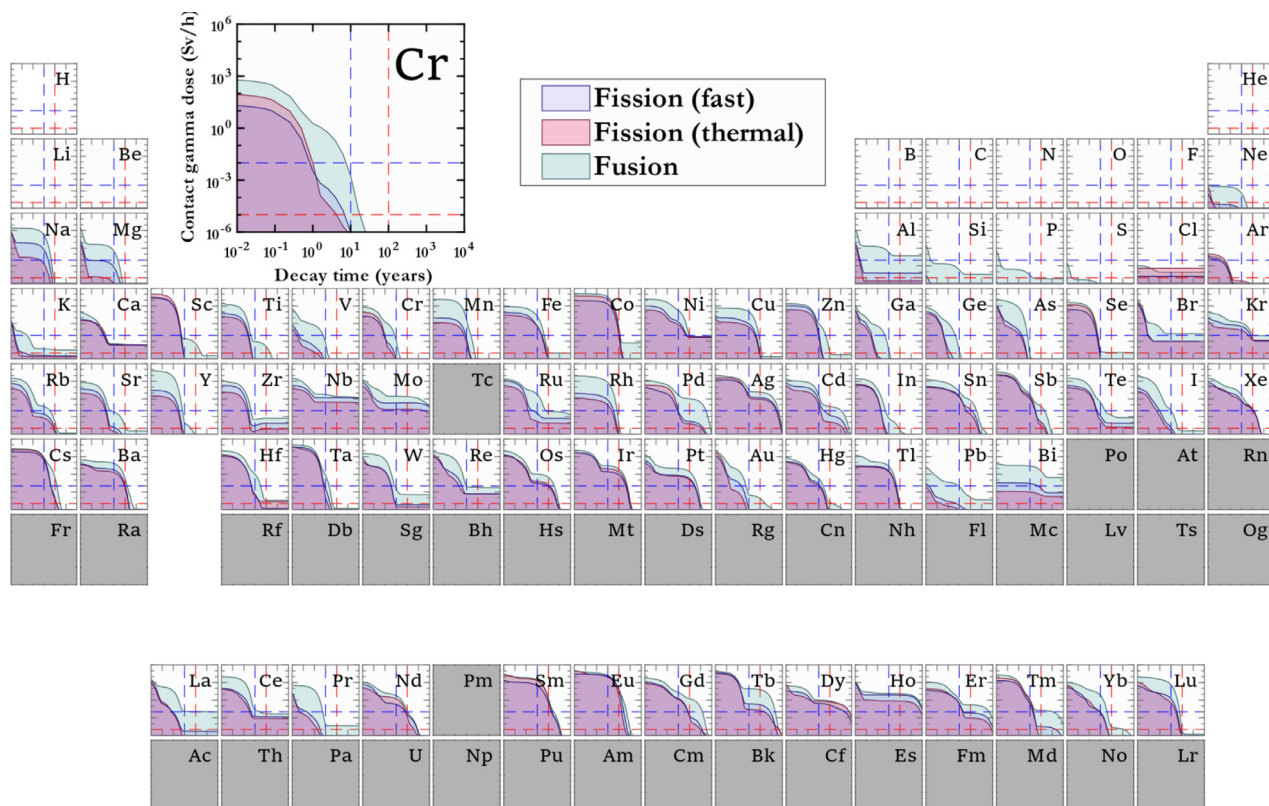


Fig. 4. Radiological activation characteristics by element (up to Bi), irradiated for 5 years under different irradiation conditions. The 'thermal' and 'fast' fission conditions emulate in-core irradiation in a PWR and SFR, respectively, while the fusion condition emulates first-wall irradiation in a DEMO-like reactor. The inset expansion of Cr defines the axes limits for all elements. The red and blue dashed lines indicate the remote recycling and "hands-on" limits, defined at 10 mSv h^{-1} after 10 years and $10 \mu\text{Sv h}^{-1}$ after 100 years, respectively. The complete dataset for this figure is linked in the 'Data availability' section.

short half-lives and very small capture cross sections. Low-Z elements do exhibit significant beta activity, however, as beta irradiation is significantly self-shielded (i.e., only β -particles emitted near the surface of a component will leave the material), beta radiation dose is not included in Fig. 4. The reported gamma dose rate represents the dose received when touching an infinitely wide and deep wall of material only attenuated by self-shielding. Maintaining distance from the active material and using shielding can drastically reduce the dose rate.

Elements irradiated under fusion conditions exhibit more activation than either fission condition and elements irradiated under fast fission conditions often exhibit slightly more activation than thermal fission – primarily due to the larger total flux of the fast fission condition – although many elements including Co, Cr, and Sc exhibit greater activation under the thermal condition due to increased neutron capture of low-energy neutrons and different activation pathways. C/C and SiC/SiC composites demonstrate a clear advantage with regards to low activation, as do several refractory elements, with V and Cr performing particularly well after all irradiation conditions, and Ti, Sc and Y reducing to hands-on activity remarkably quickly when irradiated under fission conditions. Mg and Al can exhibit a relatively low initial activity or long-term activity, respectively, under fission irradiation conditions; however, they experience greatly reduced performance under fusion irradiation. Although the high and long-lived gamma dose rate of irradiated Co is well known, Fig. 4 shows that Ag, Sn, and Sb exhibit similarly high profiles. Zn, Sc, and the several refractory elements – namely Hf, Ta, and W – also exhibit extremely high initial gamma dose rates, albeit ‘cooling’ at a faster rate. Nb, Ni and Mo remain near or above the remote recycling limit even after 10,000 years of decay. Some elements, such as Mn, Y, and Rh vary significantly based on the irradiation profile they were exposed to and may not be considered low-activation depending on the application.

The results represent pure elements at natural isotopic abundance. They do not account for elemental impurities which can drastically alter the activity profile. EUROFER reduced-activation ferritic-martensitic (RAFM) steel for fusion reactors [78], sets strict impurity limits; however, tens to hundreds of ppm of undesirable elements such as Nb, Ni, and Co are still contained in the final material which largely influence its activity. Enhanced material synthesis processes, especially in terms of elemental and isotopic separation, would greatly decrease the amount of intermediate level waste generated.

HEAs such as CrMnFeCoNi (FCC) and TiZrNbHfTa (BCC) will perform poorly in terms of gamma dose rate due to inclusion of Co or Nb. Kareer *et al.* [79] developed two low activation MEAs by replacing Nb in TiVNbTa with Cr or Zr. The resultant TiVCrTa and TiVZrTa exhibited a majority BCC structure with minor secondary phases, high hardness values of ~ 7 GPa and reduced irradiation-hardening compared to TiVNbTa and pure V, indicating good irradiation-damage tolerance. TiVZrTaW and TiVZrHfTa HEAs were studied by Ayyagari *et al.* [80,81]. After arc-melting, the TiVZrTaW alloy exhibited a single BCC phase structure with uniform grains and a hardness of ~ 6.3 GPa, while the TiVZrHfTa alloy exhibited two BCC phases in dendritic formation with a hardness of ~ 8 GPa. Ion-irradiation and mechanical testing of TiVZrHfTa showed better irradiation-hardening resistance compared to 304 stainless steel ($\sim 20\%$ increase vs. $\sim 50\%$ increase in hardness, respectively). TiVZrHfTa may be unsuitable for nuclear reactor applications due to the large neutron capture cross section of Hf. Waseem *et al.* [82] investigated spark-plasma-sintered $W_x(\text{TiVCrTa})_{1-x}$ ($x = 0.2$ to 1) alloys as reduced activation HEAs for plasma-facing fusion applications, finding multiple phases formed in the equimolar HEA along with a large increase of hardness (from ~ 3 – 5 GPa to ~ 6 – 8 GPa) compared to pure W. Five VCrFeTa $_x$ W $_x$ HEAs ($x = 0.1, 0.2, 0.3, 0.4, 1$) were investigated by Zhang *et al.* [83] exhibiting mul-

tiply BCC phases and, at higher Ta/W content, precipitation of a Laves phase. The alloys of $x = 0.1$ and 0.2 , which exhibit the least amount of Laves phase, demonstrated impressive ultimate compressive strengths over ~ 3000 MPa at compressive strains of 35–40% before their plastic limit was reached, and they retained good strength and ductility up to 800°C . Higher Ta and W content greatly increases the hardness (from ~ 5.5 to 11 GPa) and the $x = 0.3, 0.4$ and 1 alloys exhibited reduced ultimate compressive strengths between ~ 700 – 1800 MPa.

Considering their capacity to retain mechanical properties at high temperature alongside their low activation properties, HEAs consisting of the refractory elements Ti, V and Cr may be considered high-value investigations for advanced nuclear applications. The V-4Cr-4Ti alloy was applied in fusion reactor first walls due to these properties [84], however, V-4Cr-4Ti exhibits significant hardening and embrittlement during low-temperature irradiation [85] and further embrittlement during oxygen ingress [86], limiting the reactor coolant used to liquid Li. Zr, which exhibits higher but still acceptable levels of activation, provides significant benefit due to its high neutron transparency. Elements which emit significant gamma dose need not be excluded from low activity material but may be added in smaller quantities where they contribute to the improvement of the material's properties, such as small additions of Al for corrosion-resistance. $V_{35}\text{Ti}_{35}\text{Fe}_{15}\text{Cr}_{10}\text{Zr}_5$ studied by Xian *et al.* [11] exhibited two BCC phases in both as-cast and annealed conditions, and high strength which increased until 500°C . Compared to several other low activation steels, this alloy exhibited a yield strength more than 500 MPa higher in the temperature range between 500 – 700°C , though its ductility was relatively low below 700°C with only $\sim 4\%$ compressive strain to failure at room temperature. RAFM steels are currently considered primary candidates for first wall and blanket structural material in fusion reactors; however, they are limited by their elevated temperature strength and have a maximum operating temperature around 550°C . In comparison, TiVCrFeZr HEAs can potentially provide high temperature strength and possibly enhanced creep resistance due to the alloy's higher melting temperature, enabling increased operating temperature. The inclusion of Fe in such a HEA does notably elevate both the short and long-term gamma dose rate; however, Fe still exhibits a reduced gamma dose rate compared to many other elements suitable for HEAs.

3.2.2. Ashby maps to minimize activation

Ashby maps can assist the design of materials to optimize (minimize) both short- and long-term activation. Fig. 5 and Fig. 6 plot key material groups and several HEAs by their volumetric dose rate, $\dot{\Psi}$, and tensile strength, σ_T , after irradiation under thermal fission conditions and a subsequent decay period of 10 days and 100 years, respectively, representing a relatively short reactor shut down for maintenance purposes and an intermediate storage period for decommissioned reactor component cool-down before processing. The dashed lines in both figures represent the point source gamma dose rate, \dot{H} , according to the following relationship (derived in Appendix A2):

$$\dot{H} \propto \frac{\dot{\Psi}}{\sigma_T} \quad (7)$$

After 10 days of cooling, the highest gamma dose rates seen in HEAs are due to Co and Ta content, exhibiting a remarkable ~ 3 orders of magnitude higher gamma dose rate than the other HEAs. After 100 years of cooling, Nb and Ni are the most common contributors to high dose rates. Two existing HEAs display remarkably low dose rates after 100 years of decay: $\text{Al}_{20}\text{Be}_{20}\text{Fe}_{10}\text{Si}_{15}\text{Ti}_{35}$ and $\text{V}_{35}\text{Ti}_{35}\text{Fe}_{15}\text{Cr}_{10}\text{Zr}_5$. The ‘HEA potential’ circle is adapted from section 3.1 to represent a range of volumetric gamma dose rates for elemental mixtures of low dose rate elements considered appro-

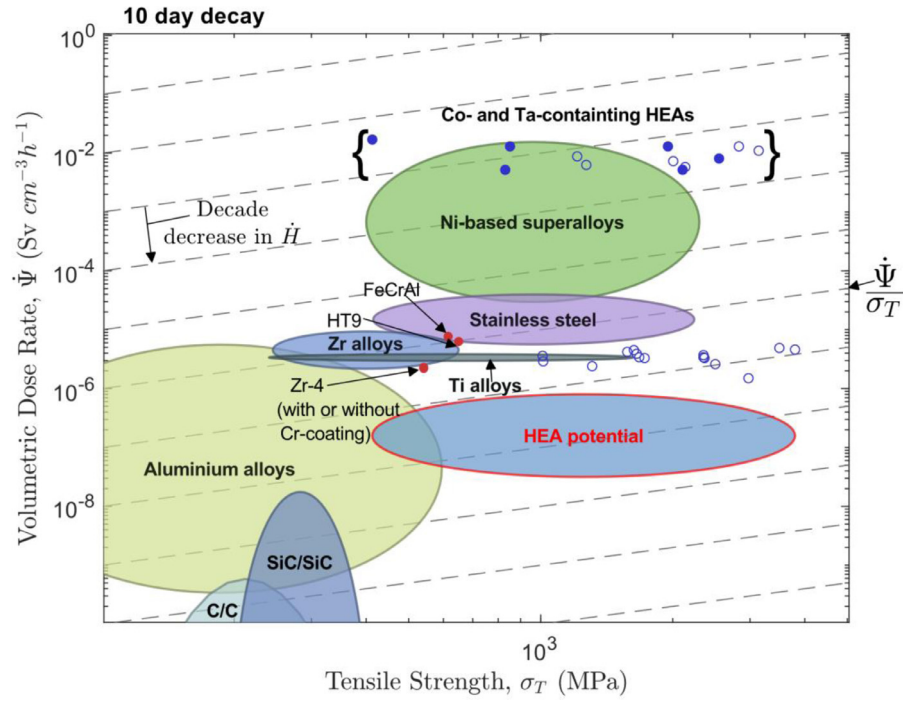


Fig. 5. Tensile strength vs. volumetric dose rate for irradiated materials decayed for 10 days. Existing high-entropy alloys are plotted as blue dots (hollow dots are used where only compressive data is available) while potential HEAs are represented as a range, optimized for minimum volumetric dose rate. Dashed lines represent constant gamma dose rate for RPVs constrained by burst pressure. Each new line proceeding lower and to the right indicates a decade decrease in gamma dose rate.

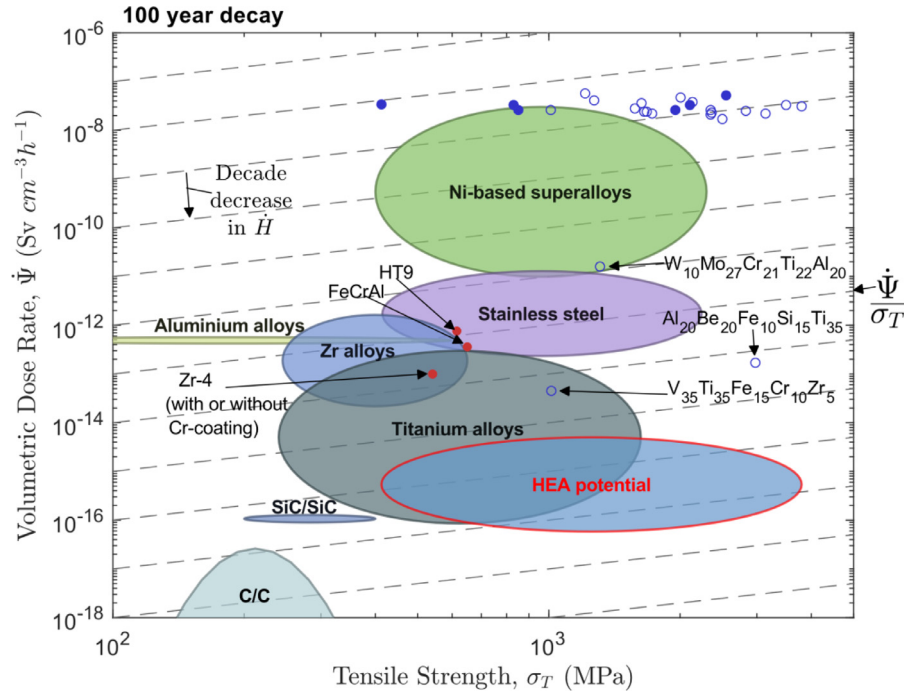


Fig. 6. Tensile strength vs. volumetric dose rate for irradiated materials decayed for 100 years. Existing high-entropy alloys are plotted as blue dots (hollow dots are used where only compressive data is available) while potential HEAs are represented as a range, optimized for minimum volumetric dose rate. Dashed lines represent constant gamma dose rate for RPVs constrained by burst pressure. Each new line proceeding lower and to the right indicates a decade decrease in gamma dose rate.

appropriate for use in nuclear applications (namely, Be, Mg, Ti, V, Cr, Zr, Ta, Al, and Fe). Similar to the minimization of neutron capture, no current HEA exists within the 'HEA potential' region due both to both limited development of HEAs containing only the species mentioned above and a lack of mechanical testing for existing HEAs. Two MEAs, TiVZrTa and TiVCrTa [80], exist with the 'HEA potential' region, exhibiting volumetric dose rates of 9.4×10^{-15}

and $2.5 \times 10^{-16} \text{ Sv cm}^{-3} \text{ h}^{-1}$, respectively, under the given irradiation conditions and a 100 year decay period. Such dose rates are extremely low, rivalling SiC/SiC composites, however, the tensile properties of these alloys have yet to be characterized.

C/C and SiC/SiC composites are superior in minimizing short- and long-term gamma dose rate for an RPV constrained by burst pressure, exhibiting several orders of magnitude less gamma dose

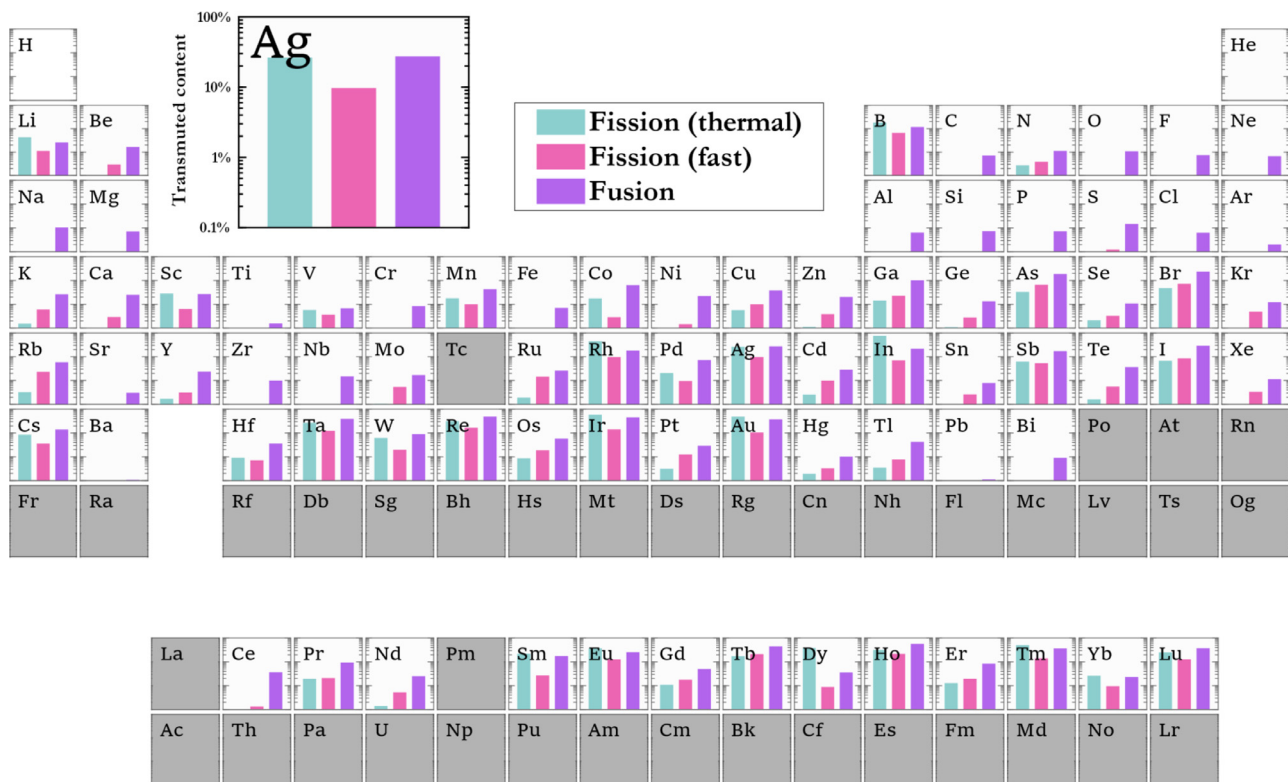


Fig. 7. Transmuted content of naturally occurring elements (up to Bi), irradiated for 5 years under different irradiation conditions. The thermal and fast fission conditions emulate in-core irradiation in a PWR and SFR, respectively, while the fusion condition emulates first-wall irradiation in a DEMO-like reactor. Bars reaching the top or bottom of the element box represent complete loss or >99.9% retention, respectively, of the original element composition after irradiation. The inset expansion of Ag defines the axis limits for each for all elements. The complete dataset for this figure is linked in the 'Data availability' section.

rate than several other alloy families. Al alloys show low short-term dose rates, however, they exhibit little decay over time which, combined with the relatively low yield strength, puts Al alloys among the highest dose options after 100 years. Ti alloys exhibit suitably low dose rates after a 10 day decay and can be some of the best options after 100 years, however, while pure titanium exhibits extremely low dose rate after 100 years, common alloying additions such as Al are responsible for its wide spread of dose rates. While Ti is extremely desirable under the given low-dose fission conditions, Fig. 4 shows that under high-dose fusion conditions Ti exceeds the hands-on dose limit at 100 years.

3.3. Alloy composition stability

Transmutation occurs in reactor materials and alters alloy compositions. This impacts the material's mechanical and functional properties. Transmutation can improve properties, such as W transmutation to Re improving ductility [82]. Transmutation is generally undesired and negatively impacts material properties. To retain a stable composition over the irradiation period, elements with a low rate of transmutation to other elements should be selected. An alternative strategy is to pair species that transmute into one another. For instance, in a neutron irradiated Cr-Mn-Fe alloy, Cr and Fe nuclides exhibit high compositional stability, and ^{55}Mn transmutes into ^{56}Fe . Fig. 7. shows the transmuted content of elements irradiated under fusion and fission conditions for 5 years. To take Ag as an example; if 1 kg of the metal was irradiated under thermal fission conditions for 5 years, 26% of the original material would transmute to other elements – in this example, the stable isotopes ^{107}Ag and ^{109}Ag would activate by neutron capture (n, γ) followed by beta decay (β^-) to produce ^{108}Cd and ^{110}Cd , respectively.

Common structural metals Fe, Cr, Al, and Ti have high compositional stability over the irradiation period. Others such as Co and Mn exhibit a greater dependency on the irradiation conditions. Of the refractory elements, desirable due to their high melting temperatures, Ti, Cr, Zr and Nb have high compositional stability under neutron irradiation, while V, Mo, Hf, Os and especially W see slightly greater losses under fission irradiation. Ta, Re, and Ir experience enormous transmutative losses.

Equally important to the fraction of transmutation products, is the chemical species of these products. For instance, a small fraction of gaseous transmutation products may have a greater impact on the alloy performance than a large fraction of a highly soluble metal species with similar alloy properties. For this reason, the transmutation of W in a fusion neutron flux may still be considered acceptable as it transmutes into refractories Re and Os which have little impact on its mechanical properties in low quantities (i.e., before the formation of a brittle σ -phase forms at 6% Os or 28% Re concentration [87]). Ta has been suggested as an alternative to W to retard the generation of Re and Os [87]. Transmutation products are as critical as remaining amounts of the initial element and the impact of some impurities on properties may be orders of magnitude greater than others. Further details on these transmutation products can be found in [88].

3.4. Formation of a nuclear HEA

The provided Ashby scatter plots allow comparison of material performance with respect to critical nuclear properties, showing where HEAs may prove competitive with industry-standard materials in specific nuclear applications, such as low cross section fuel cladding with enhanced burn-up, residence time, and accident tol-

erance compared to Zr alloys. To aid in design of a HEA for these applications, the provided nuclear property charts allow for an initial down-selection of potentially suitable elements. Further trade-off analysis, however, will be required where physical, chemical, and nuclear properties are in compromise. Other considerations may be the inclusion of self-passivating elements such as Cr, Al, and/or Ti to resist the often-corrosive reactor environments, or of refractory elements to improve mechanical performance at heightened operating temperatures.

While our theoretical design of a nuclear HEA has focused on element-specific properties, the synthesis of elements into an alloy shifts the focus to alloy-specific properties [39,89]. The production of a desirable phase or phases is dependent on several factors with complex interactions, such as enthalpic and entropic contributions of competing phases, electron configuration, and atomic size and electronegativity mismatch of the constituents, amongst others. After initial down-selection of elements, a large array of design methodologies can be applied to predict the synthesized alloy's final microstructure and mechanical properties, such as Hume-Rothery type rules [90–93], calculation of phase diagrams (CALPHAD) methodologies [39,94], the natural mixing approach [95,96], and computational methods such as density functional theory (DFT) [91], molecular dynamics (MD) [91], and machine learning (ML) [97].

4. Summary

Development of advanced structural materials in nuclear reactors can improve their safety, sustainability, economy, and public acceptance, and can in some cases be requisite for the successful implementation of future nuclear technologies with increasingly challenging operating environments. High-entropy alloys (HEAs) can exhibit impressive mechanical and thermomechanical performance suitable for such high-temperature environments, alongside several intrinsic phenomena, such as their complex energy landscape, which show promise in resisting irradiation-induced damage and promoting defect recombination.

In this work, a method of comparing key nuclear data (i.e., gamma dose rate over decay period and elemental transmutation) is provided in the form of periodic tables to aid in initial down-selection of elements for the creation of new nuclear HEAs, with elements Ti, V, Cr, and Zr showing promise across various nuclear applications due to their refractory nature, reduced activation characteristics, transmutation resistance and relatively low neutron capture cross sections. Furthermore, a method of comparing the competitiveness of existing and potential HEAs with current nuclear alloys is implemented in the form of Ashby material selection maps which establish relationships between mechanical and nuclear properties, allowing a more deliberate comparison between different alloys. Using this method, existing HEAs such as $V_{35}Ti_{35}Fe_{15}Cr_{10}Zr_5$ and $Al_{20}Be_{20}Fe_{10}Si_{15}Ti_{35}$ show competitiveness with current 'gold-standard' nuclear alloys such as Zr-4 and FeCrAl in terms of gamma dose rate after 10–100 years of decay, while potential future HEAs (i.e., those consisting of various combinations of Be, Mg, Si, Zr, Al and to a lesser extent Zn, Nb, Mo, Fe, Cr, Cu, Ni, V and Ti) are likely to compete in terms of neutron absorption rate. Investigations into the AlBeFeSiTi system (i.e., the lightweight HEA $Al_{20}Be_{20}Fe_{10}Si_{15}Ti_{35}$) may show promise in performing as well or better than Zr alloys and other alloys used for their low neutron absorption, however, neither $Al_{20}Be_{20}Fe_{10}Si_{15}Ti_{35}$ nor any other alloy of the AlBeFeSiTi system have been appropriately characterized, providing an opportunity for further studies. With the use of these tools, future HEA designs can be optimized for specific applications, facilitating further insight into their promising radiation-tolerant phenomena.

Data availability

The dataset for Fig. 4, Fig. 7 is available at doi:[10.1016/j.jnucmat.2022.153814](https://doi.org/10.1016/j.jnucmat.2022.153814). Further findings are available from the corresponding author upon reasonable request.

Declaration of Competing Interest

The authors declare that they have no known competing financial interests or personal relationships that could have appeared to influence the work reported in this paper.

CRediT authorship contribution statement

Michael Moschetti: Conceptualization, Data curation, Investigation, Methodology, Visualization, Writing – original draft. **Patrick A. Burr:** Investigation, Validation, Writing – review & editing. **Edward Obbard:** Investigation, Validation, Writing – review & editing. **Jamie J. Kruzic:** Supervision, Writing – review & editing. **Bernd Gludovatz:** Project administration, Conceptualization, Supervision, Writing – review & editing.

Acknowledgements

MM acknowledges support of an Australian Government Research Training Program (RTP) Scholarship and an AINSE Ltd. Residential Student Scholarship (RSS). PH is supported by the DOE Office of Nuclear Energy's Nuclear Energy Enabling Technologies Program, as part of project 19–17206 of the Advanced Methods for Manufacturing Program. BG additionally acknowledges support of the ARC Future Fellowship (project number FT190100484) and the UNSW Scientia Fellowship schemes.

Supplementary materials

Supplementary material associated with this article can be found, in the online version, at doi:[10.1016/j.jnucmat.2022.153814](https://doi.org/10.1016/j.jnucmat.2022.153814).

Appendix A

A1 Transmutation and decay calculations

Calculations of transmutation, activation and decay were performed with the ORIGEN (Oak Ridge Isotope GENeration) module of the SCALE 6.2.3 nuclear safety analysis and design suite. ORIGEN uses the JEFF-3.0/A neutron activation file for reaction cross sections, and the ENDF/B-VII.1 file for decay and gamma emission calculations. Two fission conditions and one fusion irradiation conditions were applied to each element with natural abundance up to Bi ($Z = 83$). The neutron flux, ϕ , of the thermal and fast fission conditions emulate irradiation of in-core components in a typical PWR ($\phi = 10^{14} \frac{n}{cm^2s}$; [98]) and SFR ($\phi = 10^{15} \frac{n}{cm^2s}$; [99,100]), respectively, while the fusion condition emulates irradiation of the plasma-facing material in a DEMO-like, D-T fusion reactor ($\phi = 10^{15} \frac{n}{cm^2s}$; [101]). Fig. A1, illustrates the neutron energy spectra, taken from [73], which are converted to 238-group spectra for use with ORIGEN. Each element is irradiated for a period of 5 years, then set to decay up to ten thousand years. Calculations account for (α, n) reactions and spontaneous fission.

A2 Ashby map relationships

Channel boxes
See Fig. A2.

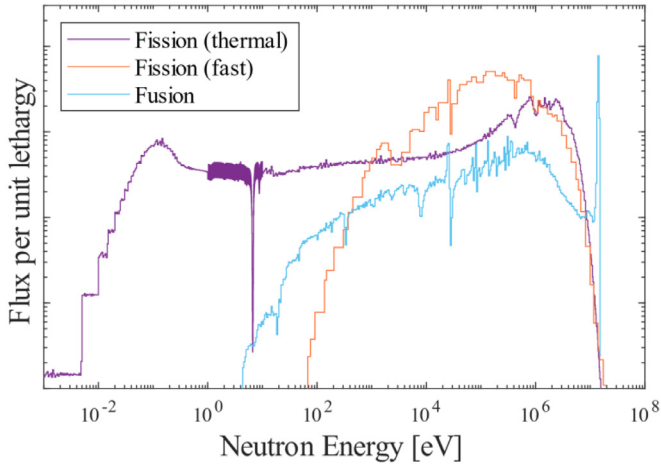


Fig. A1. Neutron spectra of fission and fusion irradiation conditions

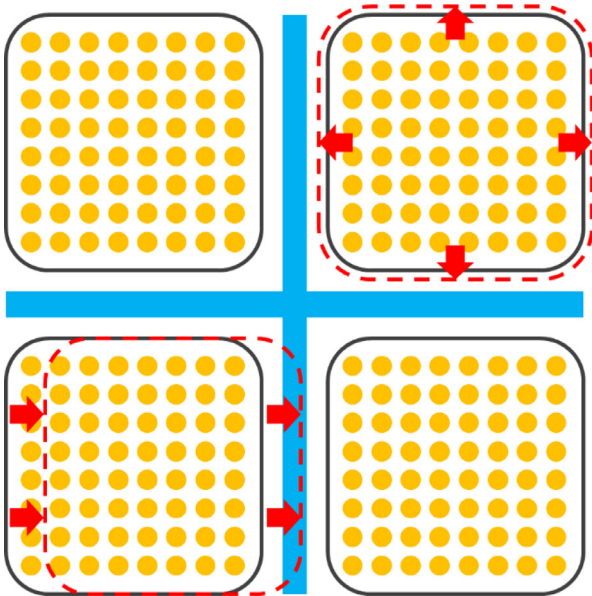


Fig. A2. A top-down schematic view of a BWR core, containing several fuel rods (yellow) inside of 4 channel boxes (black) separated by a control blade (blue). The dashed lines demonstrate two channel box failure mechanisms; bulging (top right) and bowing (bottom left) which can be seen to intersect the control blade.

Failure by bulging

For simplification, the maximum pressure of a square tube is used (ASME VIII appendix 13; [102]); the stress maxima occurring at the corners, defined by:

$$\sigma_t = \sigma_m + \sigma_b = \frac{Pb}{2t} + \frac{Pb^2}{2t^2} \quad (8)$$

where σ_t , σ_m and σ_b are the total, membrane and bending stresses, respectively, P is the pressure, and b and t are the box width and thickness, respectively. The membrane stress can be neglected as it is significantly smaller than the bending stress for thin-walled channels. Taking the thin-walled cross-sectional area as $A = 4bt$,

the same method as that described in Section 3.1 can be applied to extract the relationship:

$$R_a = \left\{ 2\sqrt{2}b^2l\Phi\sqrt{P} \right\} \left\{ \frac{\Sigma_a}{\sqrt{\sigma_T}} \right\} \quad (9)$$

Failure by bowing

Following the standard buckling equation:

$$F = \frac{n\pi^2 EI}{l^2} \quad (10)$$

where n is a buckling constant depending on the boundary conditions, E is the material's Young's modulus, and I is the second moment of area which can be simplified for a thin-walled box to be $I = 5tb^3/12$, the same method as that described in Section 3.1 can be applied to extract the relationship:

$$R_a = \left\{ \frac{48Fl^3\Phi}{5\pi^2nb^2} \right\} \left\{ \frac{\Sigma_a}{E} \right\} \quad (11)$$

Minimization of gamma dose rate

The point source gamma dose rate, \dot{H} ($Sv h^{-1}$), for each material is determined from the sum of its constituent elements:

$$\dot{H} = V \times \dot{\Psi} = 2\pi r t l \times \rho \sum \left(\frac{\dot{h}_{mol_{el}}}{M_{el}} \right) \quad (12)$$

where ρ is the density ($g cm^{-3}$) and $\dot{\Psi}$ is the volumetric gamma dose rate of the material ($Sv cm^{-3} h^{-1}$). $\dot{h}_{mol_{el}}$, c_{el} , and M_{el} are the molar point source gamma dose rate ($Sv mol^{-1} h^{-1}$), concentration (atomic ratio) and molar mass ($g mol^{-1}$) of each constituent element, respectively. The remaining variables are consistent with Eqn. (1). Molar point source gamma dose rate, $\dot{h}_{mol_{el}}$, is given by:

$$\dot{h}_{mol_{el}} = C \sum_{i=1}^{N_y} \frac{\mu_a(E_i)}{4\pi r^2} e^{-\mu(E_i)r} S_{\gamma_{mol}}(E_i) \quad (13)$$

where r is the distance to the point source (here $r = 1 m$). For each energy group, E_i , μ is its energy attenuation coefficient for air (m^{-1} ; obtained from [74]) and $S_{\gamma_{mol}}$ is the gamma energy emission rate per mole of the active material ($MeV mol^{-1} s^{-1}$) which is obtained from neutron activation calculations. The remaining variables are consistent with Eqn. (6). As the RPV is constrained by burst pressure in the same way that fuel pins area, substituting thickness for that of the rearranged Eqn. (2) gives the following relationship:

$$\dot{H} = \left\{ 2\pi r^2 t l P \right\} \left\{ \frac{\dot{\Psi}}{\sigma_T} \right\} \quad (14)$$

A3 Tabulated HEA properties

The below table lists the input and output properties used in the Ashby maps of this paper. The failure strength, σ_F , is given in tension (T) or compression (C).

Alloy	σ_F [MPa]	T/C	ρg [cm ⁻³]	E [GPa]	Σa [cm ⁻¹]	$\dot{\Psi} S v$ [cm ⁻³ h ⁻¹]		References
						10 days	100 years	
CrMnFeCoNi	851	T	7.9	203	1.03	1.32E-2	2.57E-08	[103,104]
CrMnFeCoNi ^(SPD)	1950	T	7.9	20	1.03	1.32E-2	2.57E-08	[104,105]
CrCoFeNi	413	T	8.3 ¹	-	1.04	1.72E-2	3.36E-08	[106]
AlCoCrFeNi	2830	C	7.7 ¹	127	0.87	1.28E-2	2.49E-08	[107]
AlCoCrFeNiTi _{0.5}	3140	C	7.4 ¹	178	0.82	1.12E-2	2.19E-08	[107]
TiZrNbHfTa	830	T	9.9	-	1.33	5.16E-3	3.29E-08	[108,109]
TiZrNbHfTa ^(SPD)	2106	T	9.9	79	1.34	5.18E-3	3.30E-08	[109,110]
ZrNbHfTa	2550 ²	T	12.5 ¹	-	1.74	8.12E-3	5.18E-08	[111]
TiZrNbMo	3500 ²	C	7.9 ¹	-	0.15	4.90E-6	3.29E-08	[70]
TiZrNbMoV _{0.25}	3800 ²	C	7.9 ¹	-	0.15	4.63E-6	3.11E-08	[70]
TiZrNbMoV ₃	2500 ²	C	7.3 ¹	-	0.23	2.60E-6	1.74E-08	[70]
MoNbCrVTi	1677	C	7.3	-	0.23	3.40E-6	2.43E-08	[112]
MoNbCrZrTi	1655	C	7.3	-	0.15	3.91E-6	2.44E-08	[112]
NbMoTaW	1211	C	13.8	220	0.64	8.81E-3	5.72E-08	[12,113]
VNbMoTaW	1270	C	12.4	180	0.59	6.33E-3	4.11E-08	[12,113]
TiNbMoTaW	2005	C	14.2 ¹	139	0.69	7.29E-3	4.73E-08	[114]
TiVNbMoTaW	2135	C	13.6 ¹	150	0.67	5.80E-3	3.76E-08	[114]
AlTiCrNbMo	1010	C	7.7 ¹	-	0.19	3.61E-6	2.58E-08	[14]
NbTiVZr	2350 ^{2,3}	C	6.3	86	0.17	3.69E-6	2.63E-08	[115,116]
NbTiVZr ₂	2350 ^{2,3}	C	6.4	81	0.13	3.42E-6	2.12E-08	[115,116]
CrNbTiZr	1575	C	6.7	120	0.15	4.21E-6	2.77E-08	[116]
CrNbTiVZr	1725	C	6.6	100	0.18	3.32E-6	2.18E-08	[116]
Mo _{0.5} VNbTi	1631	C	7.6	-	0.26	4.48E-6	3.60E-08	[117]
Mo _{0.5} VNbTiCr ₂	2363	C	7.5	-	0.26	3.32E-6	2.25E-08	[117]
Al ₂₀ Be ₂₀ Fe ₁₀ Si ₁₅ Ti ₃₅	2976 ⁴	-	3.9	-	0.17	1.51E-6	1.67E-13	[71]
V ₃₅ Ti ₃₅ Fe ₁₅ Cr ₁₀ Zr ₅	1013	C	6.0	-	0.32	2.87E-6	4.51E-14	[118]
W ₁₀ Mo ₂₇ Cr ₂₁ Ti ₂₂ Al ₂₀	1310	C	7.6	-	0.29	2.35E-6	1.60E-11	[119]
FeCrAl	650	T	7.6 ¹	199	0.22	6.34E-6	3.57E-13	[120,121]
HT9	615	T	7.9 ¹	-	0.23	7.71E-6	7.65E-13	[122]
Zircaloy 4	541	T	6.55	99	8.7E-3	2.27E-6	1.02E-13	[123]
Zr4 (Cr coated) ⁵	541	T	6.55	99	1.3E-2	2.24E-6	9.89E-14	[123,124]

¹ Calculated by rule of mixtures of elemental composition.

² Values interpreted from figure.

³ Values taken at 50% compressive strain, where test was stopped without sample failure.

⁴ Yield strength – estimated by $HV = 3\sigma_y$.

⁵ Assuming thin Cr-coating has no effect on strength or density.

^(SPD) Processed by severe plastic deformation.

References

- [1] T. Allen, J. Busby, M. Meyer, D. Petti, Materials challenges for nuclear systems, *Mater. Today* 13 (12) (2010) 14–23, doi:10.1016/S1369-7021(10)70220-0.
- [2] R.L. Klueh, A.T. Nelson, Ferritic/martensitic steels for next-generation reactors, *J. Nucl. Mater.* 371 (2007) 37–52, doi:10.1016/j.jnucmat.2007.05.005.
- [3] S. Ukai, M. Fujiwara, Perspective of ODS alloys application in nuclear environments, *J. Nucl. Mater.* 307–311 (2002) 749–757, doi:10.1016/S0022-3115(02)01043-7.
- [4] Y. Katoh, et al., Current status and recent research achievements in SiC/SiC composites, *J. Nucl. Mater.* 455 (2014) 387–397, doi:10.1016/j.jnucmat.2014.06.003.
- [5] K.L. Murty, I. Charit, Structural materials for Gen-IV nuclear reactors: challenges and opportunities, *J. Nucl. Mater.* 383 (2008) 189–195, doi:10.1016/j.jnucmat.2008.08.044.
- [6] E.P. George, D. Raabe, R.O. Ritchie, High-entropy alloys, *Nat. Rev. Mater.* 4 (2019) 515–534, doi:10.1038/s41578-019-0121-4.
- [7] B. Gludovatz, et al., Exceptional damage-tolerance of a medium-entropy alloy CrCoNi at cryogenic temperatures, *Nat. Commun.* 7 (10602) (2016), doi:10.1038/ncomms10602.
- [8] X.W. Qiu, Microstructure and properties of AlCrFeNiCoCu high entropy alloy prepared by powder metallurgy, *J. Alloys Compd.* 555 (2013) 246–249, doi:10.1016/j.jallcom.2012.12.071.
- [9] Z. Zhang, et al., Dislocation mechanisms and 3D twin architectures generate exceptional strength-ductility-toughness combination in CrCoNi medium-entropy alloy, *Nat. Commun.* 8 (14390) (2017), doi:10.1038/ncomms14390.
- [10] Y.P. Wang, B.S. Li, M.X. Ren, C. Yang, H.Z. Fu, Microstructure and compressive properties of AlCrFeCoNi high entropy alloy, *Mater. Sci. Eng. A* 491 (2008) 154–158, doi:10.1016/j.msea.2008.01.064.
- [11] X. Xian, et al., A high-entropy V35Ti35Fe15Cr10Zr5 alloy with excellent high-temperature strength, *Mater. Des.* 121 (2017) 229–236, doi:10.1016/j.matdes.2017.02.029.
- [12] O.N. Senkov, G.B. Wilks, J.M. Scott, D.B. Miracle, Mechanical properties of Nb25Mo25Ta25W25 and V20Nb20Mo20Ta20W20 refractory high entropy alloys, *Intermetallics* 19 (5) (2011) 698–706, doi:10.1016/j.intermet.2011.01.004.
- [13] B. Gludovatz, A. Hohenwarter, D. Catoor, E.H. Chang, E.P. George, R.O. Ritchie, A fracture-resistant high-entropy alloy for cryogenic applications, *Science* 345 (6201) (2014) 1153–1158, doi:10.1126/science.1254581.
- [14] H. Chen, et al., Microstructure and mechanical properties at elevated temperatures of a new Al-containing refractory high-entropy alloy Nb-Mo-Cr-Ti-Al, *J. Alloys Compd.* 661 (2016) 206–215, doi:10.1016/j.jallcom.2015.11.050.
- [15] C.H. Chen, Y.J. Chen, J.J. Shen, Microstructure and Mechanical Properties of (TiZrHf50)(NiCoCu)50 High Entropy Alloys, *Met. Mater. Int.* 26 (2019) 617–629, doi:10.1007/s12540-019-00383-3.
- [16] T.K. Tsao, et al., The high temperature tensile and creep behaviors of high entropy superalloy, *Sci. Rep.* 7 (1) (2017) 12658, doi:10.1038/s41598-017-13026-7.
- [17] Y. Shi, B. Yang, P. Liaw, Corrosion-resistant high-entropy alloys: a review, *Metals* 7 (2) (2017) 43, doi:10.3390/met7020043.
- [18] C.M. Liu, H.M. Wang, S.Q. Zhang, H.B. Tang, A.L. Zhang, Microstructure and oxidation behavior of new refractory high entropy alloys, *J. Alloys Compd.* 583 (2014) 162–169, doi:10.1016/j.jallcom.2013.08.102.
- [19] Q. Ye, et al., Microstructure and corrosion properties of CrMnFeCoNi high entropy alloy coating, *Appl. Surf. Sci.* 396 (2017) 1420–1426, doi:10.1016/j.apsusc.2016.11.176.
- [20] E.J. Pickering, A.W. Carruthers, P.J. Barron, S.C. Middleburgh, D.E.J. Armstrong, A.S. Gandy, High-Entropy Alloys for Advanced Nuclear Applications, *Entropy* 23 (98) (2021), doi:10.3390/e23010098.
- [21] C. Lu, et al., Enhancing radiation tolerance by controlling defect mobility and migration pathways in multicomponent single-phase alloys, *Nat. Commun.* 7 (13564) (2016), doi:10.1038/ncomms13564.
- [22] Y. Zhang, T. Egami, W.J. Weber, Dissipation of radiation energy in concentrated solid-solution alloys: unique defect properties and microstructural evolution, *MRS Bull.* 44 (10) (2019) 798–811, doi:10.1557/mrs.2019.233.
- [23] M. Sadeghilaridjani, S. Muskeri, M. Pole, S. Mukherjee, High-temperature nano-indentation creep of reduced activity high entropy alloys based on 4-5-6 elemental palette, *Entropy* 22 (230) (2020), doi:10.3390/e22020230.
- [24] O.N. Senkov, S.L. Semiatin, Microstructure and properties of a refractory high-entropy alloy after cold working, *J. Alloys Compd.* 649 (2015) 1110–1123, doi:10.1016/j.jallcom.2015.07.209.
- [25] S.J. Zinkle, J.T. Busby, Structural materials for fission & fusion energy, *Mater. Today* 12 (11) (2009) 12–19, doi:10.1016/S1369-7021(09)70294-9.
- [26] H. Zohm, Edge localized modes (ELMs), *Plasma Phys. Control. Fusion* 38 (2) (1996) 105–128, doi:10.1088/0741-3335/38/2/001.
- [27] S.J. Zinkle, L.L. Snead, Designing radiation resistance in materials for fusion energy, *Annu. Rev. Mater. Res.* 44 (1) (2014) 241–267, doi:10.1146/annurev-matsci-070813-113627.

- [28] J.W. Yeh, et al., Nanostructured high-entropy alloys with multiple principal elements: novel alloy design concepts and outcomes, *Adv. Eng. Mater.* 6 (5) (2004) 299–303, doi:[10.1002/adem.200300567](https://doi.org/10.1002/adem.200300567).
- [29] Y. Zhang, et al., Influence of chemical disorder on energy dissipation and defect evolution in concentrated solid solution alloys, *Nat. Commun.* 6 (8736) (2015), doi:[10.1038/ncomms9736](https://doi.org/10.1038/ncomms9736).
- [30] J.W. Yeh, Recent progress in high-entropy alloys, *Ann. Chim. Sci. Matér.* 31 (6) (2006) 633–648, doi:[10.3166/acsm.31.633-648](https://doi.org/10.3166/acsm.31.633-648).
- [31] Z. Wang, W. Qiu, Y. Yang, C.T. Liu, Atomic-size and lattice-distortion effects in newly developed high-entropy alloys with multiple principal elements, *Intermetallics* 64 (2015) 63–69, doi:[10.1016/j.intermet.2015.04.014](https://doi.org/10.1016/j.intermet.2015.04.014).
- [32] M. Jin, P. Cao, M.P. Short, Thermodynamic mixing energy and heterogeneous diffusion uncover the mechanisms of radiation damage reduction in single-phase Ni-Fe alloys, *Acta Mater.* 147 (2018) 16–23, doi:[10.1016/j.actamat.2017.12.064](https://doi.org/10.1016/j.actamat.2017.12.064).
- [33] R.E. Stoller, Primary radiation damage formation, *Compr. Nucl. Mater.* (2012) 293–322.
- [34] OECD Nuclear Energy Agency Primary Radiation Damage in Materials, 2015 NEA/NSC/DOC(2015)9. Accessed: Nov. 12, 2018. [Online]. Available <https://www.oecd-nea.org/science/docs/2015/nea-doc2015-9.pdf>.
- [35] K. Nordlund, et al., Improving atomic displacement and replacement calculations with physically realistic damage models, *Nat. Commun.* 9 (1) (2018) 1084, doi:[10.1038/s41467-018-03415-5](https://doi.org/10.1038/s41467-018-03415-5).
- [36] H.S. Oh, et al., Engineering atomic-level complexity in high-entropy and complex concentrated alloys, *Nat. Commun.* 10 (2090) (2019), doi:[10.1038/s41467-019-10012-7](https://doi.org/10.1038/s41467-019-10012-7).
- [37] C. Parkin, et al., In situ microstructural evolution in face-centered and body-centered cubic complex concentrated solid-solution alloys under heavy ion irradiation, *Acta Mater.* 198 (2020) 85–99, doi:[10.1016/j.actamat.2020.07.066](https://doi.org/10.1016/j.actamat.2020.07.066).
- [38] S.J. Zinkle, Radiation-Induced effects on microstructure, *Compr. Nucl. Mater.* 1 (2012) 65–98.
- [39] D.B. Miracle, O.N. Senkov, A critical review of high entropy alloys and related concepts, *Acta Mater.* 122 (2017) 448–511, doi:[10.1016/j.actamat.2016.08.081](https://doi.org/10.1016/j.actamat.2016.08.081).
- [40] K.Y. Tsai, M.H. Tsai, J.W. Yeh, Sluggish diffusion in Co–Cr–Fe–Mn–Ni high-entropy alloys, *Acta Mater.* 61 (13) (2013) 4887–4897, doi:[10.1016/j.actamat.2013.04.058](https://doi.org/10.1016/j.actamat.2013.04.058).
- [41] J. Dąbrowa, W. Kucza, G. Cieślak, T. Kulik, M. Danielewski, J.W. Yeh, Interdiffusion in the FCC-structured Al–Co–Cr–Fe–Ni high entropy alloys: experimental studies and numerical simulations, *J. Alloys Compd.* 674 (2016) 455–462, doi:[10.1016/j.jallcom.2016.03.046](https://doi.org/10.1016/j.jallcom.2016.03.046).
- [42] Y.N. Osetsky, L.K. Béland, A.V. Barashev, Y. Zhang, On the existence and origin of sluggish diffusion in chemically disordered concentrated alloys, *Curr. Opin. Solid State Mater. Sci.* 22 (3) (2018) 65–74, doi:[10.1016/j.cossms.2018.05.003](https://doi.org/10.1016/j.cossms.2018.05.003).
- [43] A. Roy, J. Munshi, G. Balasubramanian, Low energy atomic traps sluggish the diffusion in compositionally complex refractory alloys, *Intermetallics* 131 (107106) (2021), doi:[10.1016/j.intermet.2021.107106](https://doi.org/10.1016/j.intermet.2021.107106).
- [44] M. Vaidya, K.G. Pradeep, B.S. Murty, G. Wilde, S.V. Divinski, Bulk tracer diffusion in CoCrFeNi and CoCrFeMnNi high entropy alloys, *Acta Mater.* 146 (2018) 211–224, doi:[10.1016/j.actamat.2017.12.052](https://doi.org/10.1016/j.actamat.2017.12.052).
- [45] M. Vaidya, K.G. Pradeep, B.S. Murty, G. Wilde, S.V. Divinski, Radioactive isotopes reveal a non sluggish kinetics of grain boundary diffusion in high entropy alloys, *Sci. Rep.* 7 (12293) (2017), doi:[10.1038/s41598-017-12551-9](https://doi.org/10.1038/s41598-017-12551-9).
- [46] W. Kucza, J. Dąbrowa, G. Cieślak, K. Berent, T. Kulik, M. Danielewski, Studies of “sluggish diffusion” effect in Co–Cr–Fe–Mn–Ni, Co–Cr–Fe–Ni and Co–Fe–Mn–Ni high entropy alloys; determination of tracer diffusivities by combinatorial approach, *J. Alloys Compd.* 731 (2018) 920–928, doi:[10.1016/j.jallcom.2017.10.108](https://doi.org/10.1016/j.jallcom.2017.10.108).
- [47] Q. Li, W. Chen, J. Zhong, L. Zhang, Q. Chen, Z.K. Liu, On sluggish diffusion in FCC Al–Co–Cr–Fe–Ni high-entropy alloys: an experimental and numerical study, *Metals* 8 (16) (2017), doi:[10.3390/met810016](https://doi.org/10.3390/met810016).
- [48] K. Jin, C. Zhang, F. Zhang, H. Bei, Influence of compositional complexity on interdiffusion in Ni-containing concentrated solid-solution alloys, *Mater. Res. Lett.* 6 (5) (2018) 293–299, doi:[10.1080/21663831.2018.1446466](https://doi.org/10.1080/21663831.2018.1446466).
- [49] W.Y. Chen, X. Liu, Y. Chen, J.W. Yeh, K.K. Tseng, K. Natesan, Irradiation effects in high entropy alloys and 316H stainless steel at 300°C, *J. Nucl. Mater.* 510 (2018) 421–430, doi:[10.1016/j.jnucmat.2018.08.031](https://doi.org/10.1016/j.jnucmat.2018.08.031).
- [50] N.A.P.K. Kumar, C. Li, K.J. Leonard, H. Bei, S.J. Zinkle, Microstructural stability and mechanical behavior of FeNiMnCr high entropy alloy under ion irradiation, *Acta Mater.* 113 (2016) 230–244, doi:[10.1016/j.actamat.2016.05.007](https://doi.org/10.1016/j.actamat.2016.05.007).
- [51] C. Lu, et al., Enhanced void swelling in NiCoFeCrPd high-entropy alloy by indentation-induced dislocations, *Mater. Res. Lett.* 6 (10) (2018) 584–591, doi:[10.1080/21663831.2018.1504136](https://doi.org/10.1080/21663831.2018.1504136).
- [52] T. Yang, C. Li, S.J. Zinkle, S. Zhao, H. Bei, Y. Zhang, Irradiation responses and defect behavior of single-phase concentrated solid solution alloys, *J. Mater. Res.* 33 (2018) 1–15, doi:[10.1557/jmr.2018.285](https://doi.org/10.1557/jmr.2018.285).
- [53] T. Yang, et al., Precipitation behavior of AlxCoCrFeNi high entropy alloys under ion irradiation, *Sci. Rep.* 6 (32146) (2016), doi:[10.1038/srep32146](https://doi.org/10.1038/srep32146).
- [54] S.Q. Xia, X. Yang, T.F. Yang, S. Liu, Y. Zhang, Irradiation resistance in AlxCoCrFeNi high entropy alloys, *JOM* 67 (10) (2015) 2340–2344, doi:[10.1007/s11837-015-1568-4](https://doi.org/10.1007/s11837-015-1568-4).
- [55] S. Chang, K.K. Tseng, T.Y. Yang, D.S. Chao, J.W. Yeh, J.H. Liang, Irradiation-induced swelling and hardening in HfNbTaTiZr refractory high-entropy alloy, *Mater. Lett.* 272 (127832) (2020), doi:[10.1016/j.matlet.2020.127832](https://doi.org/10.1016/j.matlet.2020.127832).
- [56] S. J. Zinkle, “Radiation effects in refractory alloys”, in *AIP Conference Proceedings*, Albuquerque, New Mexico (USA), 2004, vol. 699, pp. 733–740. doi:[10.1063/1.1649637](https://doi.org/10.1063/1.1649637).
- [57] B.N. Singh, A. Horwell, P. Toft, D.J. Edwards, Temperature and dose dependencies of microstructure and hardness of neutron irradiated OFHC copper, *J. Nucl. Mater.* 224 (2) (1995) 131–140, doi:[10.1016/0022-3115\(95\)00054-2](https://doi.org/10.1016/0022-3115(95)00054-2).
- [58] J.D. Hunn, E.H. Lee, T.S. Byun, L.K. Mansur, Helium and hydrogen induced hardening in 316LN stainless steel, *J. Nucl. Mater.* 282 (2000) 131–136, doi:[10.1016/S0022-3115\(00\)00424-4](https://doi.org/10.1016/S0022-3115(00)00424-4).
- [59] S.G. Ma, Creep resistance and strain-rate sensitivity of a CoCrFeNiAl0.3 high-entropy alloy by nanoindentation, *Mater. Res. Express* 6 (2019), doi:[10.1088/2053-1591/ab52c7](https://doi.org/10.1088/2053-1591/ab52c7).
- [60] D.-H. Lee, et al., Spherical nanoindentation creep behavior of nanocrystalline and coarse-grained CoCrFeMnNi high-entropy alloys, *Acta Mater.* 109 (2016) 314–322, doi:[10.1016/j.actamat.2016.02.049](https://doi.org/10.1016/j.actamat.2016.02.049).
- [61] Y. Ma, Y.H. Feng, T.T. Debela, G.J. Peng, T.H. Zhang, Nanoindentation study on the creep characteristics of high-entropy alloy films: FCC versus BCC structures, *Int. J. Refract. Met. Hard Mater.* 54 (2016) 395–400, doi:[10.1016/j.jrmhm.2015.08.010](https://doi.org/10.1016/j.jrmhm.2015.08.010).
- [62] H. Hadraha, et al., Oxide dispersion strengthened CoCrFeNiMn high-entropy alloy, *Mater. Sci. Eng. A* 689 (2017) 252–256, doi:[10.1016/j.msea.2017.02.068](https://doi.org/10.1016/j.msea.2017.02.068).
- [63] S.H. Li, J.T. Li, W.Z. Han, Radiation-Induced Helium Bubbles in Metals, *Materials* 12 (7) (2019), doi:[10.3390/ma12071036](https://doi.org/10.3390/ma12071036).
- [64] D. Chen, et al., Diffusion controlled helium bubble formation resistance of FeCoNiCr high-entropy alloy in the half-melting temperature regime, *J. Nucl. Mater.* 526 (151747) (2019), doi:[10.1016/j.jnucmat.2019.151747](https://doi.org/10.1016/j.jnucmat.2019.151747).
- [65] M. F. Ashby, *Materials Selection in Mechanical Design*, 5th ed., Butterworth-Heinemann, 2016.
- [66] P. Hosemann, D. Frazer, M. Fratoni, A. Bolind, M.F. Ashby, Materials selection for nuclear applications: challenges and opportunities, *Scr. Mater.* 143 (2018) 181–187, doi:[10.1016/j.scriptamat.2017.04.027](https://doi.org/10.1016/j.scriptamat.2017.04.027).
- [67] V.F. Sears, Neutron scattering lengths and cross sections, *Neutron News* 3 (3) (2006) 26–37, doi:[10.1080/10448639208218770](https://doi.org/10.1080/10448639208218770).
- [68] M. Eto, S. Ishiyama, H. Ugachi, K. Fukaya, S. Baba, Mechanical properties of neutron-irradiated carbon-carbon composites for plasma facing components, *J. Nucl. Mater.* 212–215 (1994) 1223–1227, doi:[10.1016/0022-3115\(94\)91025-1](https://doi.org/10.1016/0022-3115(94)91025-1).
- [69] S. Feng, et al., Irradiation effects of fiber and matrix induced by He⁺ ion for high-performance C/C composites, *ACS Appl. Nano Mater.* 2 (5) (2019) 2926–2933, doi:[10.1021/acsanm.9b00362](https://doi.org/10.1021/acsanm.9b00362).
- [70] Y. Zhang, P.K. Liaw, Alloy design and properties optimization of high-entropy alloys, *JOM* 64 (7) (2012) 830–838, doi:[10.1007/s11837-012-0366-5](https://doi.org/10.1007/s11837-012-0366-5).
- [71] K. Tseng, Y. Yang, C. Juan, T. Chin, C. Tsai, J. Yeh, A light-weight high-entropy alloy Al20Be20Fe10Si15Ti35, *Sci. China Technol. Sci.* 61 (2) (2018) 184–188, doi:[10.1007/s11431-017-9073-0](https://doi.org/10.1007/s11431-017-9073-0).
- [72] B.T. Rearden, M.A. Jessee, SCALE Code System, Oak Ridge National Laboratory, TN, USA, 2018 [Online]. Available https://www.ornl.gov/sites/default/files/SCALE_6.2.3.pdf.
- [73] M. Fleming, T. Stainer, M. Gilbert, The FISPACT-II User Manual, 2018 UK Atomic Energy Authority, UK, UKAEA-R(18)001 [Online]. Available https://fispact.ukaea.uk/_documentation/UKAEA-R18001.pdf.
- [74] S. Seltzer, XCOM-Photon Cross Sections Database, NIST Standard Reference Database 8, National Institute of Standards and Technology, 1987, doi:[10.18434/T48G6X](https://doi.org/10.18434/T48G6X).
- [75] DTJ, BGJ, Vanadium Recycling for Fusion Reactors, US Department of Energy, Idaho Falls, United States, 1994 EGG-FSP-10378 Accessed: Jul. 09, 2020 [Online]. Available https://inis.iaea.org/collection/NCLCollectionStore/_Public/25/076/25076670.pdf?r=1.
- [76] Occupational Radiation Protection, International Atomic Energy Agency, Vienna, 2018 STI/PUB/1785 [Online]. Available <https://www.iaea.org/publications/11113/occupational-radiation-protection>.
- [77] P. Rocco, M. Zucchetti, Criteria for defining low activation materials in fusion reactor applications, *Fusion Eng. Des.* 15 (1991) 235–244, doi:[10.1016/0920-3796\(92\)90042-3](https://doi.org/10.1016/0920-3796(92)90042-3).
- [78] R. Lindau, et al., Present development status of EUROFER and ODS-EUROFER for application in blanket concepts, *Fusion Eng. Des.* 75–79 (2005) 989–996, doi:[10.1016/j.fusengdes.2005.06.186](https://doi.org/10.1016/j.fusengdes.2005.06.186).
- [79] A. Kareer, J.C. Waite, B. Li, A. Couet, D.E.J. Armstrong, A.J. Wilkinson, Short communication: “Low activation, refractory, high entropy alloys for nuclear applications”, *J. Nucl. Mater.* 526 (151744) (2019), doi:[10.1016/j.jnucmat.2019.151744](https://doi.org/10.1016/j.jnucmat.2019.151744).
- [80] A. Ayyagari, R. Salloom, S. Muskeri, S. Mukherjee, Low activation high entropy alloys for next generation nuclear applications, *Materialia* 4 (2018) 99–103, doi:[10.1016/j.mta.2018.09.014](https://doi.org/10.1016/j.mta.2018.09.014).
- [81] M. Sadeghilaridjani, et al., Ion irradiation response and mechanical behavior of reduced activity high entropy alloy, *J. Nucl. Mater.* 529 (151955) (2020), doi:[10.1016/j.jnucmat.2019.151955](https://doi.org/10.1016/j.jnucmat.2019.151955).
- [82] O.A. Waseem, S.S. Kim, J.H. Lee, S.H. Hong, H.J. Ryu, *Reduced Activation W Alloys for Plasma Facing Materials*, 2016.
- [83] W. Zhang, P. Liaw, Y. Zhang, A novel low-activation VCrFeTaWx (x = 0.1, 0.2, 0.3, 0.4, and 1) high-entropy alloys with excellent heat-softening resistance, *Entropy* 20 (951) (2018), doi:[10.3390/e20120951](https://doi.org/10.3390/e20120951).
- [84] D.L. Smith, H.M. Chung, B.A. Loomis, H. Matsui, S. Votinov, W. Van Witzenburg, Development of vanadium-base alloys for fusion first-wall - blanket applications, *Fusion Eng. Des.* 29 (1995) 399–410, doi:[10.1016/0920-3796\(95\)80046-Z](https://doi.org/10.1016/0920-3796(95)80046-Z).
- [85] H. Tsai, et al., Effects of low-temperature neutron irradiation on mechanical properties of vanadium-base alloys, *J. Nucl. Mater.* 283 (2000) 362–366, doi:[10.1016/S0022-3115\(00\)00224-5](https://doi.org/10.1016/S0022-3115(00)00224-5).

- [86] B.A. Pint, J.R. DiStefano, The role of oxygen uptake and scale formation on the embrittlement of vanadium alloys, *Oxid. Met.* 63 (2005) 33–55, doi:[10.1007/s11085-005-1950-7](https://doi.org/10.1007/s11085-005-1950-7).
- [87] G.A. Cottrell, Sigma phase formation in irradiated tungsten, tantalum and molybdenum in a fusion power plant, *J. Nucl. Mater.* 334 (2004) 166–168, doi:[10.1016/j.jnucmat.2004.07.001](https://doi.org/10.1016/j.jnucmat.2004.07.001).
- [88] R.A. Forrest, A. Tabasso, C. Danani, S. Jakhar, A.K. Shaw, *Handbook of Activation Data Calculated Using EASY-2007*, 2009 UKAEA FUS 552.
- [89] Y. Zhang, et al., Microstructures and properties of high-entropy alloys, *Prog. Mater. Sci.* 61 (2014), doi:[10.1016/j.pmatsci.2013.10.001](https://doi.org/10.1016/j.pmatsci.2013.10.001).
- [90] X. Yang, Y. Zhang, Prediction of single-phase high-entropy stabilized solid-solution in multi-component alloys, *Mater. Chem. Phys.* 132 (2–3) (2012) 233–238, doi:[10.1016/j.matchemphys.2011.11.021](https://doi.org/10.1016/j.matchemphys.2011.11.021).
- [91] M. C. Gao, J.W. Yeh, P. K. Liaw, Y. Zhang, *High-Entropy Alloys*, Springer, 2016, doi:[10.1007/978-3-319-27013-5](https://doi.org/10.1007/978-3-319-27013-5).
- [92] S. Guo, C.T. Liu, Phase stability in high entropy alloys: formation of solid-solution phase or amorphous phase, *Prog. Nat. Sci. Mater. Int.* 21 (6) (2011) 433–446, doi:[10.1016/S1002-0071\(12\)60080-X](https://doi.org/10.1016/S1002-0071(12)60080-X).
- [93] M.C. Tropicovsky, J.R. Morris, P.R.C. Kent, A.R. Lupini, G.M. Stocks, Criteria for predicting the formation of single-phase high-entropy alloys, *Phys. Rev. X* 5 (011041) (2015), doi:[10.1103/PhysRevX.5.011041](https://doi.org/10.1103/PhysRevX.5.011041).
- [94] C. Zhang and M. C. Gao, 'CALPHAD modeling of high-entropy alloys', in *High-Entropy Alloys: Fundamentals and Applications*, M. C. Gao, , P. K. Liaw, and Y. Zhang, Springer, 2016. [Online]. Available: doi:[10.1007/978-3-319-27013-5_12](https://doi.org/10.1007/978-3-319-27013-5_12).
- [95] I.T.H. Chang, P. Knight, A.J.B. Vincent, Microstructural development in equiatomic multicomponent alloys, *Mater. Sci. Eng. A* 375–377 (2004) 213–218, doi:[10.1016/j.msea.2003.10.257](https://doi.org/10.1016/j.msea.2003.10.257).
- [96] S. Wei, et al., Natural-mixing guided design of refractory high-entropy alloys with as-cast tensile ductility, *Nat. Mater.* (2020), doi:[10.1038/s41563-020-0750-4](https://doi.org/10.1038/s41563-020-0750-4).
- [97] W. Huang, P. Martin, H.L. Zhuang, Machine-learning phase prediction of high-entropy alloys, *Acta Mater* 169 (2019) 225–236, doi:[10.1016/j.actamat.2019.03.012](https://doi.org/10.1016/j.actamat.2019.03.012).
- [98] United States Nuclear Regulatory Commission Westinghouse AP1000 Design Control Document Rev. 19 (Tier 2, Chapter 4, Section 4.3, 2011 [Online]. Available: www.nrc.gov/docs/ML1117/ML11171A500.html.
- [99] C. Jammes, et al., Neutron flux monitoring system of the French GEN-IV SFR: assessment of diverse solutions for in-vessel detector installation, *Nucl. Eng. Des.* 270 (2014) 273–282, doi:[10.1016/j.nucengdes.2013.12.057](https://doi.org/10.1016/j.nucengdes.2013.12.057).
- [100] P. Filliatre, C. Jammes, B. Geslot, L. Buiron, In vessel neutron instrumentation for sodium-cooled fast reactors: type, lifetime and location, *Ann. Nucl. Energy* 37 (11) (2010) 1435–1442, doi:[10.1016/j.anucene.2010.06.023](https://doi.org/10.1016/j.anucene.2010.06.023).
- [101] M.R. Gilbert, S.L. Dudarev, S. Zheng, L.W. Packer, J.C.H. Sublet, An integrated model for materials in a fusion power plant: transmutation, gas production, and helium embrittlement under neutron irradiation, *Nucl. Fusion* 52 (083019) (2012), doi:[10.1088/0029-5515/52/8/083019](https://doi.org/10.1088/0029-5515/52/8/083019).
- [102] J. R. Farr and M. H. Jawad, *Guidebook for the Design of ASME Section VIII Pressure Vessels*, 3rd ed. New York: ASME Press, 2006.
- [103] A.J. Zaddach, R.O. Scattergood, C.C. Koch, Tensile properties of low-stacking fault energy high-entropy alloys, *Mater. Sci. Eng. A* 636 (2015) 373–378, doi:[10.1016/j.msea.2015.03.109](https://doi.org/10.1016/j.msea.2015.03.109).
- [104] G. Laplanche, P. Gadaud, O. Horst, F. Otto, G. Eggeler, E.P. George, Temperature dependencies of the elastic moduli and thermal expansion coefficient of an equiatomic, single-phase CoCrFeMnNi high-entropy alloy, *J. Alloys Compd.* 623 (2015) 348–353, doi:[10.1016/j.jallcom.2014.11.061](https://doi.org/10.1016/j.jallcom.2014.11.061).
- [105] B. Schuh, et al., Mechanical properties, microstructure and thermal stability of a nanocrystalline CoCrFeMnNi high-entropy alloy after severe plastic deformation, *Acta Mater* 96 (2015) 258–268, doi:[10.1016/j.actamat.2015.06.025](https://doi.org/10.1016/j.actamat.2015.06.025).
- [106] W.H. Liu, J.Y. He, H.L. Huang, H. Wang, Z.P. Lu, C.T. Liu, Effects of Nb additions on the microstructure and mechanical property of CoCrFeNi high-entropy alloys, *Intermetallics* 60 (2015), doi:[10.1016/j.intermet.2015.01.004](https://doi.org/10.1016/j.intermet.2015.01.004).
- [107] Y.J. Zhou, Y. Zhang, Y.L. Wang, G.L. Chen, Solid solution alloys of AlCoCrFeNiTiX with excellent room-temperature mechanical properties, *Appl. Phys. Lett.* 90 (181904) (2007), doi:[10.1063/1.2734517](https://doi.org/10.1063/1.2734517).
- [108] B. Schuh, et al., Thermodynamic instability of a nanocrystalline, single-phase TiZrNbHfTa alloy and its impact on the mechanical properties, *Acta Mater* 142 (2018) 201–212, doi:[10.1016/j.actamat.2017.09.035](https://doi.org/10.1016/j.actamat.2017.09.035).
- [109] O.N. Senkov, J.M. Scott, S.V. Senkova, D.B. Miracle, C.F. Woodward, Microstructure and room temperature properties of a high-entropy TaNbHfZrTi alloy, *J. Alloys Compd.* 509 (20) (2011) 6043–6048, doi:[10.1016/j.jallcom.2011.02.171](https://doi.org/10.1016/j.jallcom.2011.02.171).
- [110] M. Moschetti, et al., On the room-temperature mechanical properties of an ion-irradiated TiZrNbHfTa refractory high entropy alloy, *JOM* (72) (2019) 130–138, doi:[10.1007/s11837-019-03861-6](https://doi.org/10.1007/s11837-019-03861-6).
- [111] S. Maiti, W. Steurer, Structural-disorder and its effect on mechanical properties in single-phase TaNbHfZr high-entropy alloy, *Acta Mater* 106 (2016) 87–97, doi:[10.1016/j.actamat.2016.01.018](https://doi.org/10.1016/j.actamat.2016.01.018).
- [112] C. Xiang, et al., Design of single-phase high-entropy alloys composed of low thermal neutron absorption cross-section elements for nuclear power plant application, *Intermetallics* 104 (2019) 143–153, doi:[10.1016/j.intermet.2018.11.001](https://doi.org/10.1016/j.intermet.2018.11.001).
- [113] O.N. Senkov, G.B. Wilks, D.B. Miracle, C.P. Chuang, P.K. Liaw, Refractory high-entropy alloys, *Intermetallics* 18 (9) (2010) 1758–1765, doi:[10.1016/j.intermet.2010.05.014](https://doi.org/10.1016/j.intermet.2010.05.014).
- [114] Z.D. Han, et al., Effect of Ti additions on mechanical properties of NbMoTaW and VNbMoTaW refractory high entropy alloys, *Intermetallics* 84 (2017) 153–157, doi:[10.1016/j.intermet.2017.01.007](https://doi.org/10.1016/j.intermet.2017.01.007).
- [115] D.J.M. King, et al., High temperature, low neutron cross-section high-entropy alloys in the Nb-Ti-V-Zr system, *Acta Mater* 166 (2019) 435–446, doi:[10.1016/j.actamat.2019.01.006](https://doi.org/10.1016/j.actamat.2019.01.006).
- [116] O.N. Senkov, S.V. Senkova, D.B. Miracle, C. Woodward, Mechanical properties of low-density, refractory multi-principal element alloys of the Cr-Nb-Ti-V-Zr system, *Mater. Sci. Eng. A* 565 (2013) 51–62, doi:[10.1016/j.msea.2012.12.018](https://doi.org/10.1016/j.msea.2012.12.018).
- [117] C. Xiang, et al., Effect of Cr content on microstructure and properties of Mo0.5VNbTiCrX high-entropy alloys, *J. Alloys Compd.* 818 (2020) 153352, doi:[10.1016/j.jallcom.2019.153352](https://doi.org/10.1016/j.jallcom.2019.153352).
- [118] X. Xian, et al., A high-entropy V35Ti35Fe15Cr10Zr5 alloy with excellent high-temperature strength, *Mater. Des.* 121 (2017) 229–236, doi:[10.1016/j.matdes.2017.02.029](https://doi.org/10.1016/j.matdes.2017.02.029).
- [119] H. Naser-Zoshki, A.R. Kiani-Rashid, J. Vahdati-Khaki, Design of a low density refractory high entropy alloy in non-equiatomic W-Mo-Cr-Ti-Al system, *Vacuum* 181 (109614) (2020), doi:[10.1016/j.vacuum.2020.109614](https://doi.org/10.1016/j.vacuum.2020.109614).
- [120] Y. Yamamoto, B.A. Pint, K.A. Terrani, K.G. Field, Y. Yang, L.L. Snead, Development and property evaluation of nuclear grade wrought FeCrAl fuel cladding for light water reactors, *J. Nucl. Mater.* 467 (2015) 703–716, doi:[10.1016/j.jnucmat.2015.10.019](https://doi.org/10.1016/j.jnucmat.2015.10.019).
- [121] Z.T. Thompson, K.A. Terrani, Y. Yamamoto, Elastic Modulus Measurement of ORNL ATF FeCrAl Alloys, Oak Ridge National Laboratory (ORNL), 2015 ORNL/TM-2015/632, doi:[10.2172/1225433](https://doi.org/10.2172/1225433).
- [122] Y. Chen, Irradiation effects of HT-9 martensitic steel, *Nucl. Eng. Technol.* 45 (3) (2013) 311–322, doi:[10.5516/NET.07.2013.706](https://doi.org/10.5516/NET.07.2013.706).
- [123] Allegheny Technologies Incorporated Technical Data Sheet: Reactor Grade Zirconium, 2015 [Online]. Available <https://www.atimetals.com/Products/zircaloy-4>.
- [124] M. Wagih, B. Spencer, J. Hales, K. Shirvan, Fuel performance of chromium-coated zirconium alloy and silicon carbide accident tolerant fuel claddings, *Ann. Nucl. Energy* 120 (2018) 304–318, doi:[10.1016/j.anucene.2018.06.001](https://doi.org/10.1016/j.anucene.2018.06.001).